iScience

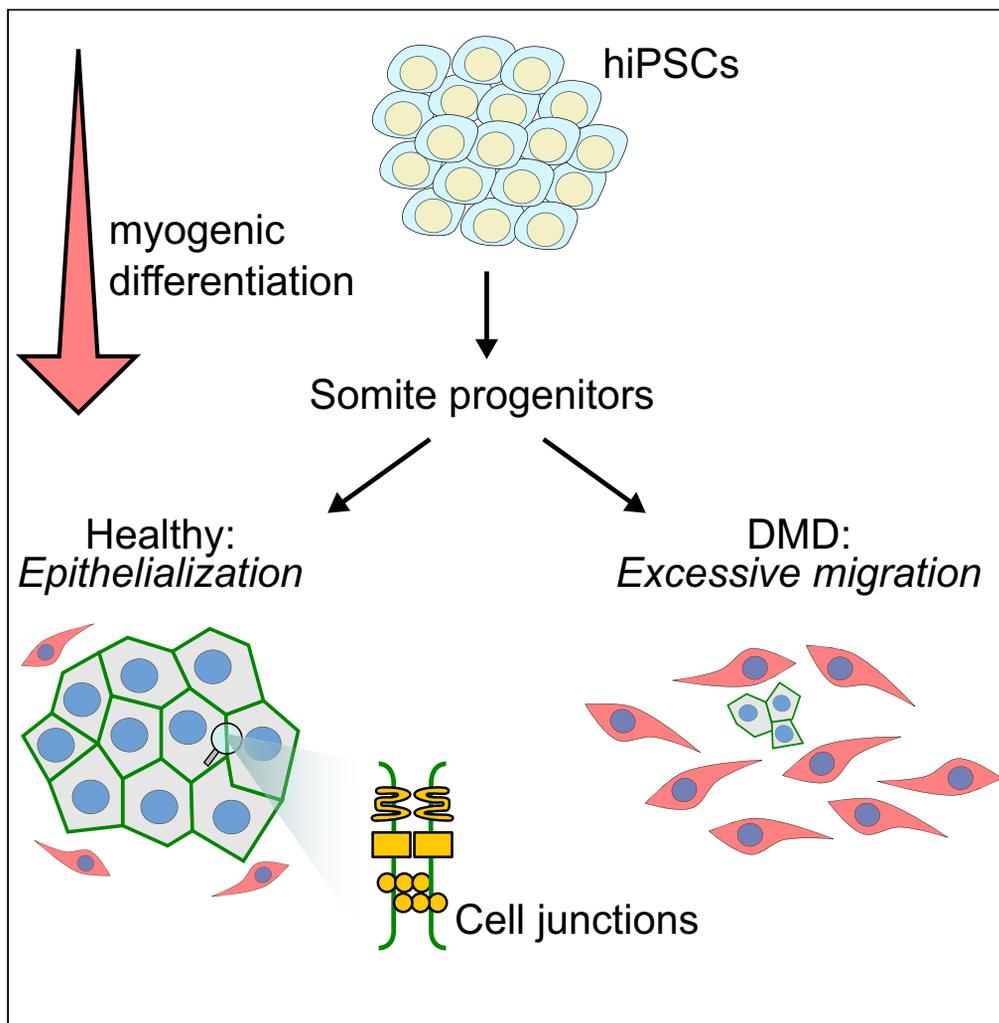**Article**

Dystrophin deficiency impairs cell junction formation during embryonic myogenesis from pluripotent stem cells

Elise Mozin,
Emmanuelle
Massouridès,
Virginie
Mournetas, ...,
Christian Pinset,
David L. Mack,
Jean-Baptiste
Dupont

jean-baptiste.dupont@
univ-nantes.fr

Highlights

Myogenic differentiation of DMD hiPSCs diverges at the somite stage

Cell junction formation is dysregulated in DMD somite cells

Somite cells from DMD hiPSCs have impaired epithelialization properties

Migration velocity of DMD-mutant somite progenitors is upregulated

Article

Dystrophin deficiency impairs cell junction formation during embryonic myogenesis from pluripotent stem cells

Elise Mozin,[1] Emmanuelle Massouridès,[2] Virginie Mournetas,[3] Clémence Lièvre,[1] Audrey Bourdon,[1] Dana L. Jackson,[4] Jonathan S. Packer,[4] Juyoung Seong,[5,6] Cole Trapnell,[4] Caroline Le Guiner,[1] Oumeya Adjali,[1] Christian Pinset,[2] David L. Mack,[6] and Jean-Baptiste Dupont[1,7,*]

SUMMARY

Mutations in the *DMD* gene lead to Duchenne muscular dystrophy (DMD), a severe neuromuscular disorder affecting young boys as they acquire motor functions. DMD is typically diagnosed at 2–4 years of age, but the absence of dystrophin has negative impacts on skeletal muscles before overt symptoms appear in patients, which poses a serious challenge in current standards of care. Here, we investigated the consequences of dystrophin deficiency during skeletal muscle development. We used single-cell transcriptome profiling to characterize the myogenic trajectory of human pluripotent stem cells and showed that DMD cells bifurcate to an alternative branch when they reach the somite stage. Dystrophin deficiency was linked to marked dysregulations of cell junction proteins involved in the cell state transitions characteristic of embryonic somitogenesis. Altogether, this work demonstrates that *in vitro*, dystrophin deficiency has deleterious effects on cell-cell communication during myogenic development, which should be considered in future therapeutic strategies for DMD.

INTRODUCTION

Mutations in genes involved in skeletal muscle functions trigger a spectrum of diseases which can lead to significant motor and respiratory impairments, sometimes shortly after birth.[1–3] The cellular and molecular mechanisms of these diseases are complex and result in the breakdown of skeletal muscle homeostasis. In Duchenne muscular dystrophy (DMD) patients, the lack of functional dystrophin causes systemic pathological perturbations, which mostly affect the skeletal muscles, heart, and central nervous system. In muscle cells, *DMD* mutations lead to sarcolemmal membrane fragility, calcium overload, oxidative stress, mitochondrial impairments, development of an inflammatory microenvironment, and a pro-fibroadipogenic process.[4] As muscles develop in the absence of dystrophin, capturing the pathological molecular cascade downstream of the mutation and tracking progression over time are difficult using animal models. Early studies described prenatal signs of muscle wasting in presymptomatic *mdx* mice and GRMD puppies.[5,6] Signs of muscle damage such as variable myotube diameter, hyaline fibers, and internal nuclei had also been observed in fetuses at risk for DMD.[7,8] The most well-characterized functions of dystrophin have been described in fully differentiated skeletal muscle cells, which express the longest isoform of the protein (Dp427m) that connects the contractile machinery with the sarcolemma and the extracellular matrix through the dystrophin-associated protein complex (DAPC).[4] In other organs, the expression of the *DMD* locus gives rise to other protein isoforms with specific N-terminal regions. How dystrophin expression arises during the embryonic development of different cell lineages remains difficult to characterize with available *in vivo* models. In the embryo, skeletal muscles emerge from the paraxial mesoderm, which differentiates into transient metameric structures called somites, and then into the dermomyotome.[9] This involves a succession of well-orchestrated cell division, migration, and transitions between epithelial and mesenchymal states that later give rise to myogenic progenitors with migratory properties.[10–12] In this context, the expression of dystrophin and the consequences of pathological mutations during skeletal muscle development remain to be characterized in a reliable model.

Pluripotent stem cells represent a proxy for human embryonic development, and they allow the characterization of early disease mechanisms in a dish.[13–15] Several groups have published protocols to differentiate human induced pluripotent stem cells (hiPSCs) into paraxial

[1]Nantes Université, CHU Nantes, INSERM, TARGET, F-44000 Nantes, France
[2]Centre d'Etude des Cellules Souches, I-Stem, AFM, F-91100 Corbeil-Essonnes, France
[3]ADLIN Science, F-91058 Evry, France
[4]Department of Genome Sciences, University of Washington School of Medicine, Seattle, WA 98105, USA
[5]Department of Biomedical Engineering, Ulsan National Institute of Science and Technology (UNIST), Ulsan 44919, South Korea
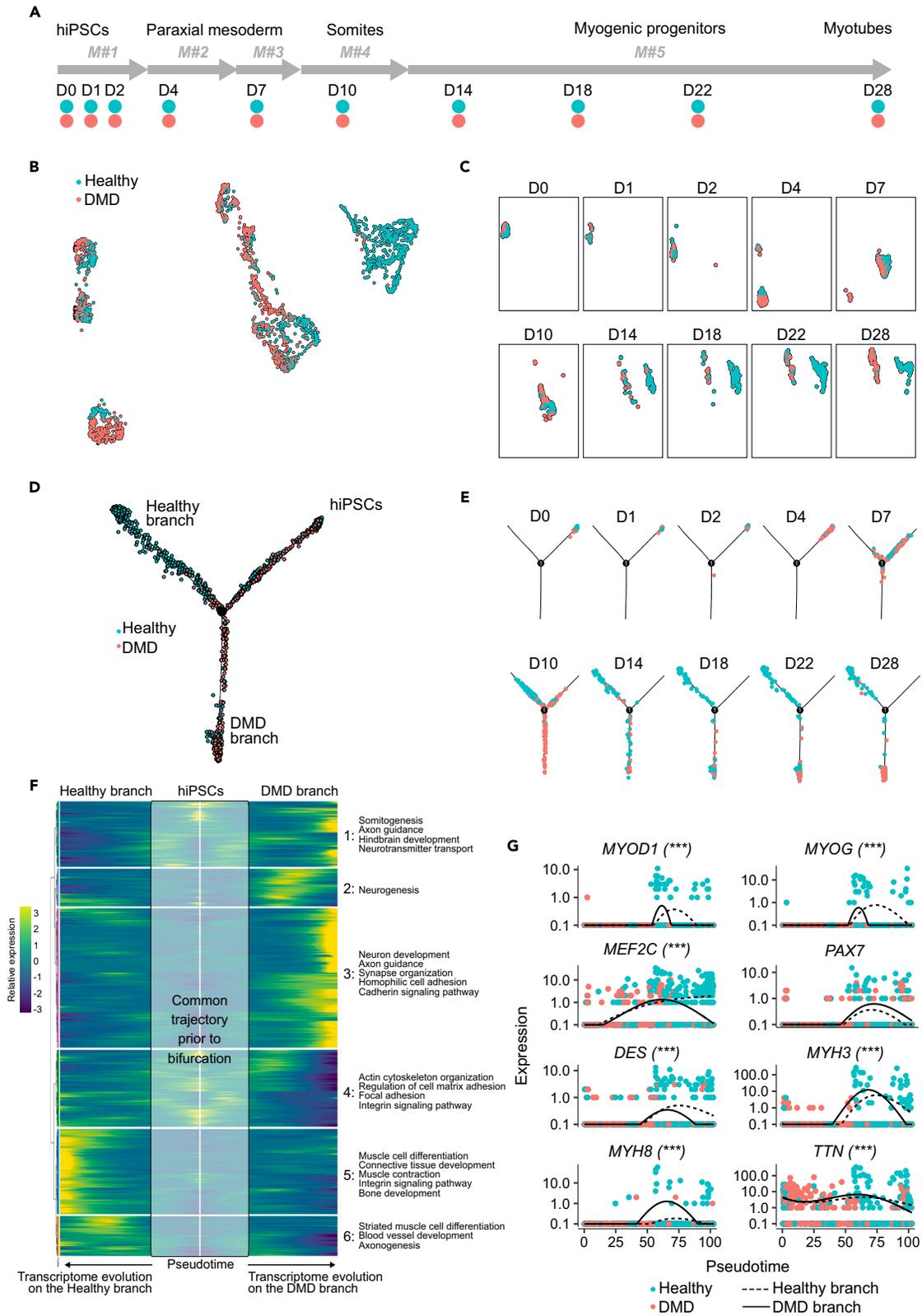[6]Institute for Stem Cell and Regenerative Medicine, Department of Rehabilitation Medicine, University of Washington, Seattle, WA 98109, USA
[7]Lead contact
*Correspondence: jean-baptiste.dupont@univ-nantes.fr
https://doi.org/10.1016/j.isci.2024.110242

A hiPSCs — M#1 — Paraxial mesoderm — M#2 — M#3 — Somites — M#4 — Myogenic progenitors — M#5 — Myotubes

D0 D1 D2   D4   D7   D10   D14   D18   D22   D28

B ● Healthy ● DMD

C D0 D1 D2 D4 D7 / D10 D14 D18 D22 D28

D Healthy branch, hiPSCs, DMD branch; ● Healthy ● DMD

E D0 D1 D2 D4 D7 / D10 D14 D18 D22 D28

F Healthy branch | hiPSCs | DMD branch

Relative expression (3, 2, 1, 0, -1, -2, -3)

1: Somitogenesis / Axon guidance / Hindbrain development / Neurotransmitter transport

2: Neurogenesis

3: Neuron development / Axon guidance / Synapse organization / Homophilic cell adhesion / Cadherin signaling pathway

Common trajectory prior to bifurcation

4: Actin cytoskeleton organization / Regulation of cell matrix adhesion / Focal adhesion / Integrin signaling pathway

5: Muscle cell differentiation / Connective tissue development / Muscle contraction / Integrin signaling pathway / Bone development

6: Striated muscle cell differentiation / Blood vessel development / Axonogenesis

Pseudotime

Transcriptome evolution on the Healthy branch ← → Transcriptome evolution on the DMD branch

G *MYOD1* (***), *MYOG* (***), *MEF2C* (***), *PAX7*, *DES* (***), *MYH3* (***), *MYH8* (***), *TTN* (***)

Expression — Pseudotime

● Healthy — — Healthy branch
● DMD —— DMD branch

Figure 1. DMD hiPSCs bifurcate to an alternative branch of the myogenic trajectory at the somite stage

(A) Cell collection timeline along hiPSC myogenic differentiation using the combination of 5 defined media (M#1 to M#5) described previously.[16] D0–D28: day 0 to day 28.

(B) UMAP plot showing the 1917 individual cells colored by hiPSC line of origin.

(C) Deconvolution of the UMAP plot by collection time point (D0–D28).

(D) Single-cell trajectory capturing the dynamics of myogenic differentiation as DMD and healthy hiPSCs progress along the initial common branch (hiPSCs) to the bifurcation point (1) and one of the two alternative branches.

(E) Deconvolution of the single-cell trajectory by collection time point (D0–D28).

(F) Branched expression analysis modeling identifying modules of genes with branch-dependent expression. Key gene ontology terms associated with each individual module are indicated on the right-hand side.

(G) Gene expression kinetic in pseudotime for myogenic markers along the healthy (dotted line) and the DMD (full line) branch. Each dot shows an individual cell with its computed pseudotime value. Significant differences in branch-dependent expression are indicated with *** (p-adj < 0.001). See also Figure S1; Tables S1 and S2.

mesoderm progenitors, somite intermediates, dermomyotome, and ultimately skeletal muscle progenitors.[16–19] Recently, our group has used hiPSCs from DMD patients to demonstrate that marked transcriptome dysregulations occur prior to skeletal muscle commitment.[20] Characterization of *DMD* gene expression during early mesoderm induction had led to the identification of an embryonic isoform of dystrophin (Dp412e) in mesoderm progenitors and embryoid bodies.[21] This isoform possesses an alternative exon 1 and encodes an N-truncated protein starting in exon 6 of the skeletal muscle dystrophin isoform (Dp427m). However, its functions and molecular partners remain unknown.

Transcriptomic analysis of hiPSC derivatives at single-cell resolution offers the opportunity to shed light on complex biological processes such as embryonic development and to investigate the effects of disease-causing mutations in any given lineage intermediate. In particular, single-cell RNA-sequencing (scRNA-seq) has helped characterize the diversity of skeletal muscle cells involved in muscle development,[22,23] specification,[24,25] aging,[26–28] and in various models of DMD.[29–32] Reconstruction of single-cell trajectories thanks to pseudotemporal ordering of cells has been used to describe dynamics and gene expression profiles during differentiation of myoblasts.[33,34] Studying the divergence of this trajectory when hiPSCs harbor a mutated *DMD* gene will provide a deeper understanding of the molecular drivers of pathology immediately downstream of the mutation and the cascade of molecular events after disease initiation.

In this study, we established the single-cell trajectory of healthy and dystrophin-deficient hiPSCs subjected to myogenic differentiation. We showed that hiPSCs derived from a DMD patient diverged from healthy control cells as early as the somite stage and that the differences propagated as differentiation progressed. After inclusion of an isogenic CRISPR-engineered DMD line, we demonstrated that several cell junction gene families were markedly dysregulated as a consequence of dystrophin deficiency in somite progenitors. Further characterization identified epithelial and mesenchymal populations coexisting *in vitro*, reflecting the cell state transitions occurring in the embryo and that the formation of epithelial islets is altered in the absence of dystrophin. Finally, we confirmed our results in three additional DMD hiPSC lines by immunostaining and analysis of previous bulk RNA-seq data generated in our group, which strongly suggests that *DMD* mutations have significant consequences during prenatal development. Overall, this study indicates that dystrophin deficiency leads to disruptions of cell-cell communication and coordinated migration during somitogenesis.

RESULTS

DMD hiPSCs bifurcate to an alternative branch of the myogenic trajectory at the somite stage

Human iPSCs from a DMD patient harboring an exon 50 deletion in the *DMD* gene were subjected to directed differentiation into the skeletal muscle lineage in parallel with a healthy control,[35] using a transgene-free and serum-free protocol.[16] Microscopic monitoring showed extensive cell proliferation and densification into multilayered cultures over time (Figure S1A). The differentiation was stopped at day 28 when fields of thin and spindly myotubes could be observed in the healthy control line. To investigate the dynamics of myogenic differentiation and the impact of dystrophin deficiency, cells were isolated at ten discreet time points from day 0 (D0) to day 28 (D28), tagged with barcoded primers during *in situ* reverse-transcription and pooled for single-cell combinatorial indexing RNA-seq (sci-RNA-seq, Figure 1A).[36] A total of 1,917 individual cells could be retrieved from 20 distinct samples corresponding to the 2 hiPSC lines across 10 time points (Table S1), and used in the subsequent clustering analyses. After Uniform Manifold Approximation and Projection (UMAP) for dimension reduction, cells were distributed among 7 clusters expressing well-defined marker genes associated with pluripotency at day 0 (e.g., *POU5F1*, clusters 1–2), primitive streak at day 2 (*T*, cluster 5), paraxial mesoderm at day 2–4 (*TBX6*, cluster 3), somite and dermomyotome at day 7–10 (*PAX3*, clusters 2–7), and ultimately skeletal muscle progenitor cells from dy 22–28 (*PAX7*, *MYOD1*, cluster 1) (Figures S1B–S1D). Interestingly, DMD and healthy control cells were intermingled into superimposed clusters during the first week (day 0–7), but from day 10, they started to form distinct cell populations (Figures 1B and 1C). Single-cell trajectory reconstruction with Monocle[22,34,36] identified a bifurcation point between day 7 and day 10, from which most of the cells segregated on two distinct branches in a genotype-dependent manner (Figures 1D and 1E). More precisely, 86% of the healthy cells after the divergence were on a single branch (621 vs. 103), while 86% of the DMD cells were on the other branch (329 vs. 55, Figures S1E and S1F). Branch expression analysis modeling (BEAM) identified thousands of differentially expressed genes (DEG) along the WT and the DMD-enriched branches. The most significant candidates (1,987 genes with p-adj <0.0001) were clustered based on their expression dynamics on the two branches for gene ontology analysis (Figure 1F, Table S2). Interestingly, modules of genes overexpressed along the healthy branch were enriched for terms related to muscle development (e.g., muscle cell differentiation, muscle contraction, and actin cytoskeleton organization). In contrast, gene modules overexpressed along the DMD branch matched with gene ontology
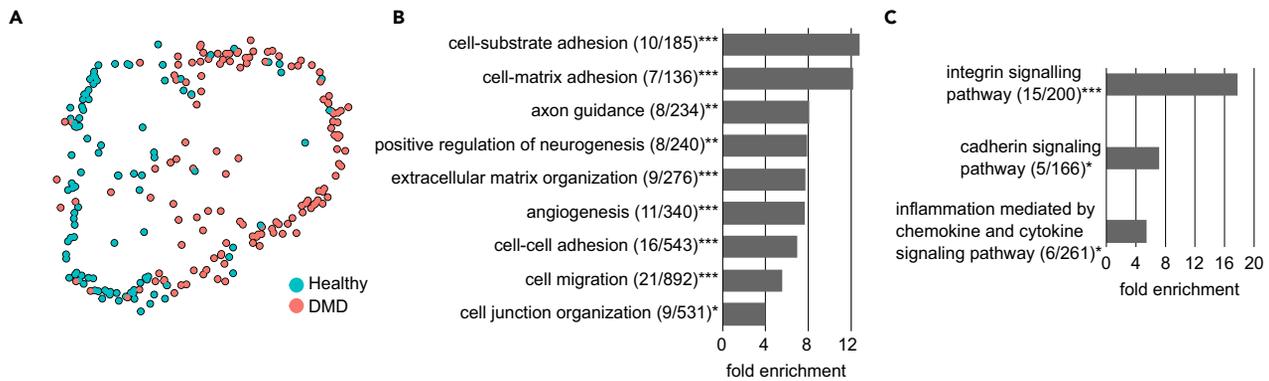
Figure 2. DMD patient-derived hiPSCs exhibit a marked dysregulation of cell junction genes at day 10

(A) UMAP plot of the individual cells collected at day 10 from the sci-RNA-seq dataset (Figure 1) colored by their hiPSC line of origin.

(B and C) Gene ontology (B) and pathway enrichment (C) analyses performed with the 94 genes differentially expressed in DMD cells at day 10 in the sci-RNA-seq dataset. Legend: * false discovery rate (FDR) < 0.05; ** FDR <0.01; *** FDR <0.001; (X/Y): number of genes from the GO category found differentially expressed in the dataset/total number of genes in the GO category. See also Table S3.

(GO) terms related to the development of alternative lineages, particularly neurons (e.g., neurogenesis, synapse organization, and axon guidance). To gain insight into the regulation of myogenesis in pseudotime, differential expression of skeletal muscle markers was assessed between the two branches. Significant differences in pseudotemporal dynamics were found for critical regulators of myogenesis, including *MYOD1*, *MYOG*, and *MEF2C*. Notably, the master regulators *MYOD1* and *MYOG* were expressed at very low levels in DMD cells, in contrast with *PAX7* and *MEF2C*, although for the latter, expression in DMD cells was significantly reduced as pseudotime progressed (Figure 1G). In addition, genes coding for important structural proteins such as *MYH3*, *MYH8*, *DES*, or *TTN* were also found significantly dysregulated (Figure 1G). Thus, hiPSCs derived from a DMD patient deviated from the myogenic trajectory followed by healthy control cells at the somite stage, resulting in dysregulated expression of myogenesis regulators.

DMD patient-derived hiPSCs exhibit a marked dysregulation of cell junction genes at day 10

As the deviation of DMD cells was first evident at day 10 on the single-cell trajectory, "day10" cells were reanalyzed separately. Although a single UMAP cluster was observed, DMD and healthy control cell were clearly separated (Figure 2A). Differential expression analysis using the regression model from Monocle 3 identified 94 genes significantly dysregulated in DMD cells (adjusted *p* value <0.01) (Table S3). Among these differentially expressed genes (DEGs), multiple cell junction and extracellular matrix genes were identified, including cadherins and proto-cadherins (*CDH11* and *PCDH9*), integrins (*ITGA1*, *ITGA4*, *ITGB1*, and *ITGAV*), fibronectin (*FN1*), and numerous collagens (*COL1A2*, *COL3A1*, and *COL4A1*, etc.). GO analysis confirmed significant enrichments in related biological processes, such as cell-matrix interaction (*p* = 5.6E-4), cell-cell adhesion (*p* = 6.9E-7), extracellular matrix organization (*p* = 6.9E-4), and cell junction organization (*p* = 4.0E-2) (Figure 2B). Strikingly, PANTHER pathway statistical enrichment test only identified 3 pathways as significantly overrepresented in the DEG list, and two of them were directly related to specific cell junction protein families: the integrin and cadherin signaling pathways (*p* = 2.4E-12 and *p* = 4.2E-2, respectively) (Figure 2C). Of note, the GO analysis also indicated that DEGs included regulators of key developmental processes in non-muscle lineages, such as neurogenesis and axon guidance (*SEMA3A*, *EPHA3*, *NRP1*, *NEFL*, and *UNC5C*) and angiogenesis (*ANGPT1*, *THSD7A*). Neuronal by-products have already been observed when hiPSCs are differentiated with this specific protocol.[37] In this study, the DMD hiPSC line might be more prone to such uncontrolled differentiation events, leading to the formation of more alternative cell types.

Dystrophin deficiency does not compromise myotube formation despite upstream dysregulation of multiple cell junction protein families

The dysregulation events triggered by dystrophin deficiency in somite progenitors were evaluated using a myogenic differentiation protocol that utilizes media formulation commercialized by amsbio and previously shown to generate a homogeneous muscle cell population.[17,20] In addition to the DMD patient hiPSC line, an isogenic DMD CRISPR line was engineered from the healthy control line by deleting the entire exon 45 of the *DMD* gene together with 17 base pairs in exon 54,[38] leading to an absence of dystrophin protein (Figure S2A). The cell lines and the differentiation protocols used at each step of this study are recapitulated in Table S4. The ability of DMD patient-derived and CRISPR-engineered dystrophin null hiPSCs to differentiate into multinucleated myotubes using the amsbio protocol was evaluated by immunofluorescence after 25 days of differentiation. Myotubes were stained for two skeletal muscle proteins: myosin heavy chains and α-actinin. Multinucleated myofibers with striations could be observed in the 3 hiPSC lines (Figures 3A and S2B). We quantified the area positive for α-actinin and obtained comparable fluorescent signals in the 3 hiPSC lines representing 34% of the total area on average (Figure 3B). Thus, overall myotube formation is not impacted by dystrophin deficiency with the amsbio protocol. Prior to terminal differentiation, hiPSCs undergo several rounds of amplification and passages as they transition through the successive developmental intermediates. In particular, a "somite"
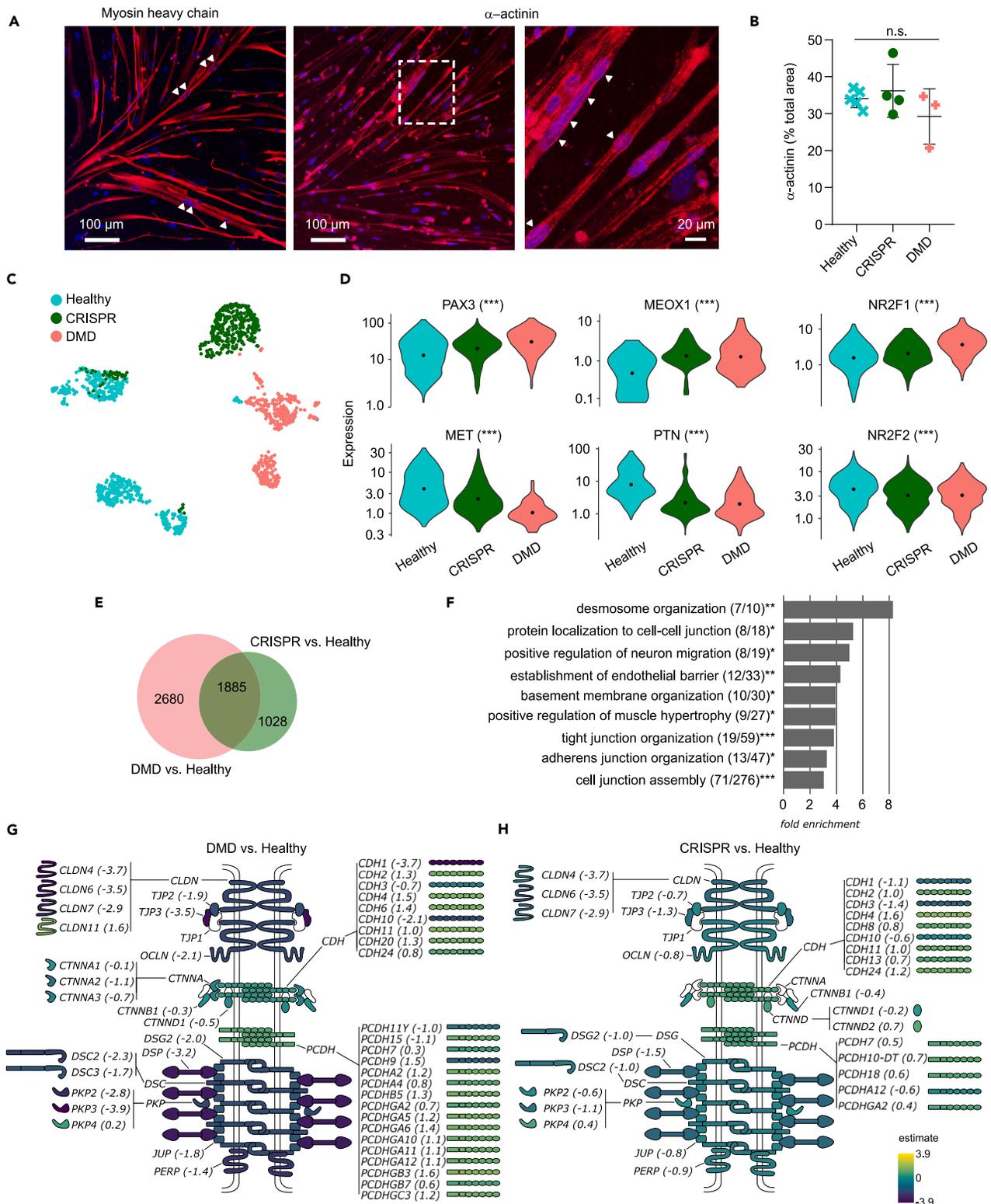
Figure 3. Dystrophin deficiency does not compromise myotube formation despite upstream dysregulation of multiple cell junction protein families

(A) Fluorescent staining of myosin heavy chains and α-actinin (red) in myotubes derived from Healthy hiPSCs. Arrowheads indicate multinucleation and the right panel focuses on a striation pattern. Scale bar, 100 μm (left and middle panels) or 20 μm (right panel).

Figure 3. *Continued*

(B) Quantification of the α-actinin fluorescent area in the three cell lines, expressed as a percentage of total area (*n* = 3 to 5 panels by cell line). Data are represented as individual dots with lines at mean ± SD.

(C) UMAP plot showing the 3,566 individual cells colored by their hiPSC line of origin.

(D) Violin plots showing the expression of somite marker genes in single cells from healthy, CRISPR, and DMD hiPSCs at day 10.

(E) Venn diagram of the differentially expressed genes in DMD and CRISPR hiPSC lines at day 10. The absolute numbers of genes are indicated in the appropriate sections.

(F) Gene ontology analysis with the 1,885 genes differentially expressed in both the DMD and the CRISPR hiPSC lines at day 10, showing a selection of significantly enriched biological processes. Legend: * false discovery rate (FDR) < 0.05; ** FDR <0.01; *** FDR <0.001; (X/Y): number of genes from the GO category found differentially expressed in the dataset/total number of genes in the GO category.

(G and H) Differential expression of cell junction genes and potential implications at the protein level in the DMD (G) and CRISPR (H) hiPSC lines. Fold change estimates from single-cell data are indicated between brackets and color-coded for each protein. CLDN, claudin; OCLN, occludin; TJP, tight junction protein; CDH, cadherin; CTNN, contactin; PCDH, protocadherin; DSG, desmoglein; DSP, desmoplakin; DSC, desmocollin; PKP, plakophilin; JUP, plakoglobin; PERP, p53 apoptosis effector related to PMP22. See also Figures S2 and S3; Tables S4 and S5.

gene expression signature was previously described by bulk RNA-seq at differentiation day 10.[20] Thus, hiPSCs were differentiated up to day 10 and analyzed by single-cell RNA-seq. After dimensional reduction, the UMAP plot revealed that DMD cells and healthy controls were separated into distant clusters. The CRISPR clusters were found in between, closer to the DMD cells with only a small fraction overlapping with healthy cells (Figure 3C). Expression of well-characterized somite marker genes such as *MET*, *PTN*, *NR2F1* and *NR2F2*, *MEOX1*, and *PAX3* was confirmed at single-cell resolution (Figure 3D). Importantly, DMD patient cells expressed significantly higher levels of *PAX3*, *MEOX1*, and *NR2F1* than healthy controls and lower levels of *MET*, *PTN*, and *NR2F2*. The CRISPR line presented with a less pronounced dysregulation profile, yet statistically significant for all the aforementioned marker genes except *NR2F1*. Absence of differentiation by-products was confirmed at day 10, with little to no expression of neural tube (*SOX2*, *PAX6*, and *IRX3*), lateral plate mesoderm (*GATA4*), intermediate mesoderm (*PAX8*), and sclerotome (*PAX1*) marker genes on the UMAP, confirming the overall purity of the cultures (Figure S3A). Differential expression analysis using the Monocle 3 pipeline identified 4,565 and 2,913 significantly dysregulated genes in the DMD patient line and the CRISPR line, respectively, when compared to the healthy control (*p*-adj <0.01, Table S5). Among these, 1,885 genes were differentially expressed in both lines, which represent the core gene set dysregulated at the somite stage as a direct consequence of the DMD deficiency (Figure 3E). Of note, this also illustrates the influence of the genetic background on disease manifestation at the transcriptome level, as 36% of the CRISPR-induced dysregulations were not present in the DMD patient line. Importantly however, the common DEGs also included 55 of the 94 genes (59%) found significantly dysregulated at Day 10 in the previous dataset (Figure 2). GO analysis on the 1,885 overlap genes showed enrichment for terms related to cell junctions, such as desmosome organization (*p* = 7.2E-3), tight junction organization (*p* = 4.4E-4), and cell junction assembly (*p* = 2.2E-11) (Figure 3F). Specific focus on key cell junction families highlighted marked down-regulations of not only tight junction genes, such as claudins (*CLDN*), ocludin (*OCLN*), and tight junction proteins (*TJP*) but also desmosome genes such as desmoplakin (*DSP*), desmogleins (*DSG*), and desmocollins (*DSC*) in the DMD line. In contrast, multiple genes from the protocadherin (*PCDH*) and cadherin (*CDH*) families were up-regulated (Figure 3G). As aforementioned, the CRISPR line showed an intermediary dysregulation profile for all cell junction protein families (Figure 3H). In the initial dataset, adherens junctions including *CDH* and *PCDH* genes were also part of the BEAM gene list (Table S2), together with genes encoding catenins (*CTNN*) (Figure S3B). Altogether, these results suggest a major role for cell junction gene families in the initiation and progression of DMD during development.

Dystrophin deficiency leads to impaired cell state transitions during *in vitro* somite development

The role of cell junction proteins in the dynamics of paraxial mesoderm development has been highlighted in multiple species, particularly in the cell state transitions happening during the formation of somites bilaterally on either side of the neural tube and later during the delamination of the dermomyotome.[10–12,39–46] Thus, hiPSC-derived somite progenitors *in vitro* might undergo successive mesenchymal-to-epithelial and epithelial-to-mesenchymal transitions accompanied by a well-coordinated remodeling of the cell-cell and cell-matrix junctions. The morphology of the hiPSC cultures was evaluated between day 7 and day 10 of the amsbio protocol. At day 10, two cell populations with distinct features were observed: (1) spindly, refringent, tightly packed cells with a mesenchymal morphology and (2) larger, more flattened cells in close contact to one another similar to squamous or cuboidal epithelia (Figure 4A). These larger cells were first detected at day 8 and progressively form islets until day 10 (Figure S4A). Immunofluorescence assays showed that the islets expressed high levels of E-cadherin (E-cad), a cell junction protein characteristic of epithelial cells and were negative for vimentin (Vim), a cytoskeleton protein expressed mostly in mesenchymal cells (Figures 4B and S4B). Conversely, the cells surrounding the islets expressed Vim but no E-cad. The fluorescent signal was quantified in the 3 hiPSC lines at day 10 and we found ∼10% E-cad-positive cells in both the healthy control line and the CRISPR line and less than 1% in the DMD line (Figure 4C). We next assessed the expression of C-Met, a receptor tyrosine kinase expressed at the membrane of epithelial cells during dermomyotome development from the somites and critical for subsequent myoblast migration.[47–49] Interestingly, we observed a strong C-Met expression in epithelial islets, suggesting a dermomyotome identity, but no C-Met-positive cell was found in the DMD line. Differentiation of the CRISPR line resulted in C-Met expression at day 10 but at a level 5 times lower than in the healthy control (p value = 0.029) (Figures 4D and 4E). This suggests that somitogenesis and the associated cell state transitions are altered in the absence of dystrophin but that additional factors have an influence, depending on the genetic background.
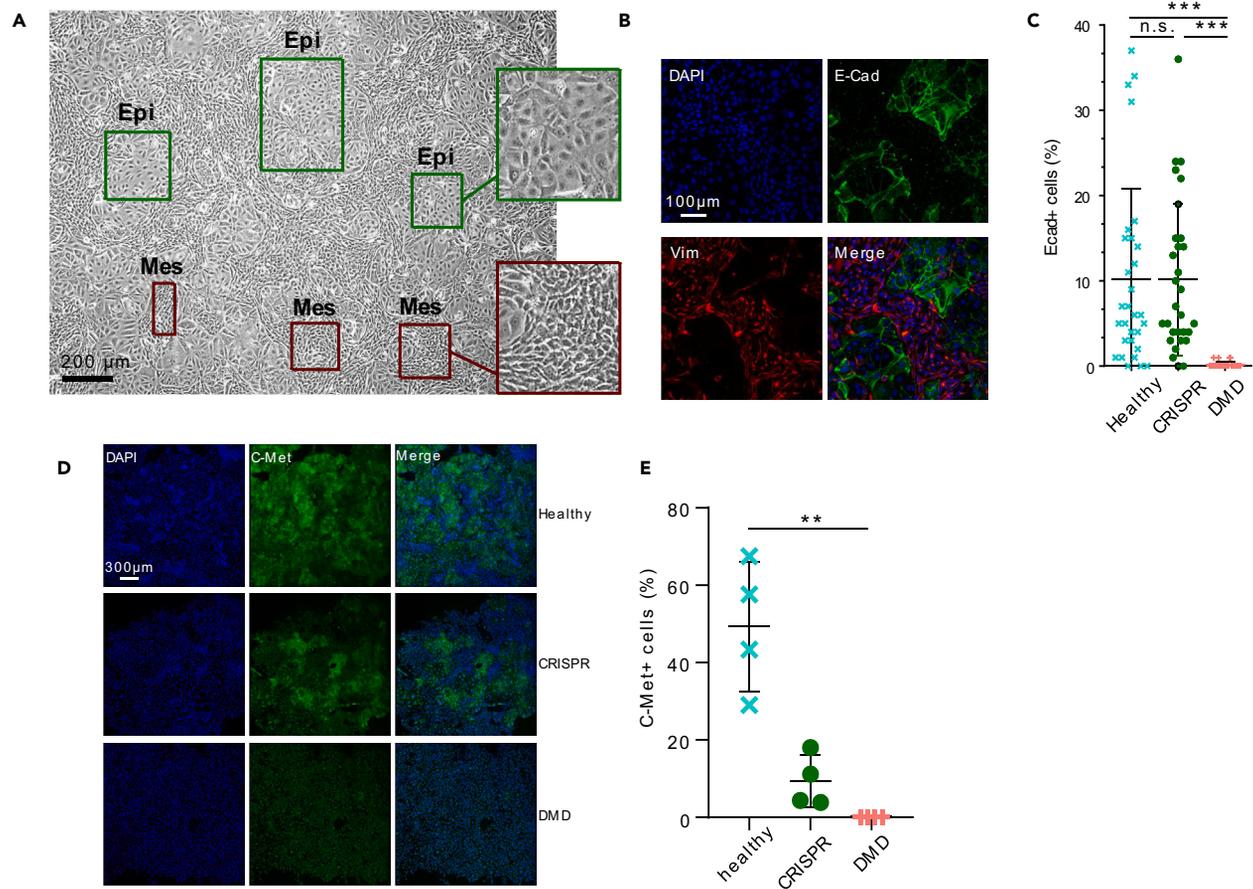
Figure 4. Dystrophin deficiency leads to impaired cell state transitions during in vitro somite development

(A) Optical microscopy with phase contrast of somite progenitors derived from hiPSCs. Insets highlight the "epithelial-like" (Epi) and "mesenchymal-like" (Mes) cell populations. Scale bar, 200μm.

(B) Detection of E-Cad and Vim in somite progenitors derived from hiPSCs by immunofluorescence and confocal microscopy. Scale bar, 100 μm.

(C) Quantification of the percentage of E-Cad-positive cells in the healthy, DMD, and CRISPR hiPSC lines at day 10 in three replicate experiments (N = 10 panels by experiment). Data are represented as individual dots with lines at mean ± SD. n.s. not significant; *** p value <0.001.

(D) Detection of C-Met in the three hiPSC lines by immunostaining and confocal microscopy at differentiation day 10. Scale bar, 300 μm.

(E) Quantification of the C-Met fluorescent area normalized by the number of nuclei. Imaging was performed on four large mosaic panels per cell line. Date are represented as individual dots with lines at mean ± SD. ** p value <0.01. See also Figure S4.

DMD-specific defects in somitogenesis and cell junction gene dysregulations are independent of the genetic background

To confirm that cell junction dysregulation during embryonic myogenesis in the absence of dystrophin was also observed in other genetic backgrounds, we compared our current findings with an RNA-seq dataset previously generated by our group that describes myogenic differentiation of DMD hiPSCs at defined time points (https://muscle-dmd.omics.ovh/).[20] More precisely, hiPSC lines from three independent DMD patients and three healthy individuals were differentiated in triplicate with the amsbio media formulation[17] and cells were collected for bulk RNA-seq at several time points (Figure S5A). Interestingly, the transcriptome of DMD hiPSCs markedly diverged from healthy controls at Day 10, when somite marker genes are expressed.[20] Immunostaining at day 10 showed the presence of epithelial islets expressing C-Met in the 6 hiPSC lines but at a level 5.7 lower in the 3 DMD patient lines, confirming the results obtained in the initial DMD patient-derived and CRISPR lines (Figures 5A and 5B). Further analysis of the RNA-seq dataset identified 1,450 genes significantly dysregulated at day 10 in the 3 DMD cell lines (abs(log2 fold-change) ≥ 1 and adjusted p value ≤0.01), among which several cell junction protein families (Figure 5C; Table S6). GO analyses showed a significant enrichment in genes involved in the formation of cell junctions (Figure 5D), which confirms their importance in the initial manifestation of DMD during somite differentiation, independently of the genetic background. Particularly, desmosome organization (GO:0002934) was affected in DMD cells, with a significant downregulation of *GRHL1* (log FC = −2.5, p value = 3.7E-06), *JUP* (log FC = −1.0, p value = 7.7E-04), *PERP* (log FC = −1.4, p value = 1.2E-08), *PKP2* (log FC = −1.5, p value = 2.6E-03) and *PKP3* (log FC = −2.9, p value = 1.1E-03) (Figure 5E). Tight junction organization (GO:0120193) was also perturbed by the absence of dystrophin, with dysregulation of gene members of the claudin (CLDN), cadherin (CDH), and protocadherin (PCDH) families (Figure 5E). Overall, cell junction genes
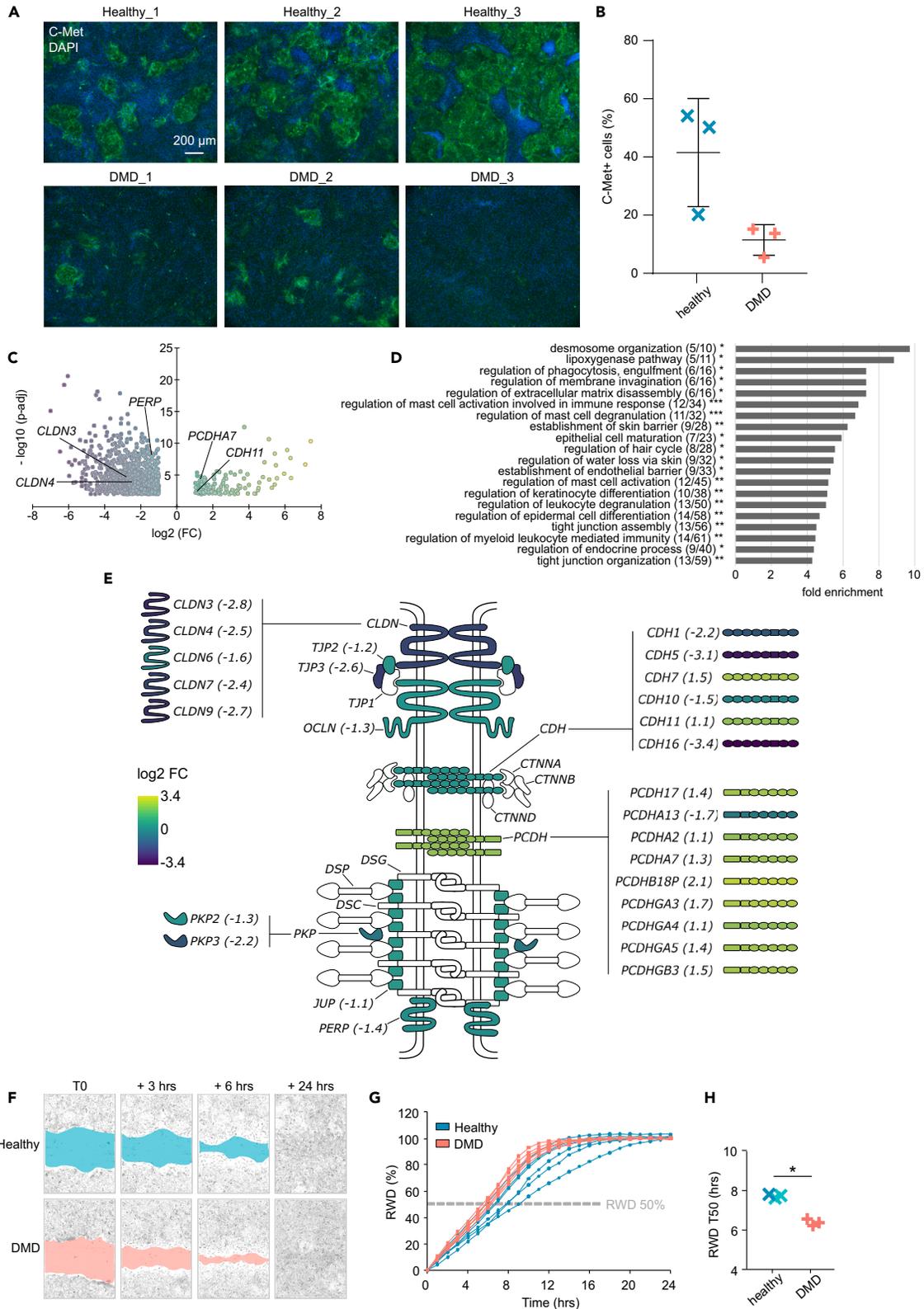
Figure 5. DMD-specific defects in somitogenesis and cell junction gene dysregulations are independent of the genetic background

(A) Fluorescent staining of C-Met in DMD hiPSCs and healthy control lines at day 10 of the myogenic differentiation. One representative picture is shown per individual line (healthy_1 to 3 and DMD_1 to 3). Scale bar, 200 μm.

(B) Quantification of the C-Met fluorescent area normalized by the number of nuclei. Imaging was performed on three independent pictures per line. Data are represented as individual dots with lines at mmean ± SD.

(C) Volcano plot of the differentially expressed genes in DMD somite progenitor cells at day 10 (thresholds: |log2 FC| > 1 and p-adj <0.01).

(D) Gene ontology analysis using the differentially expressed genes as input and showing key biological processes. Legend: * false discovery rate (FDR) < 0.05; ** FDR <0.01; *** FDR <0.001; (X/Y): number of genes from the GO category found differentially expressed in the dataset/total number of genes in the GO category.

(E) Differential expression of cell junction genes and potential implications at the protein level. Fold change values (DMD vs. healthy) are indicated between brackets and color-coded for each protein. CLDN, claudin; OCLN, occludin; TJP, tight junction protein; CDH, cadherin; CTNN, contactin; PCDH, protocadherin; DSG, desmoglein; DSP, desmoplakin; DSC, desmocollin; PKP, plakophilin; JUP, plakoglobin; PERP, p53 apoptosis effector related to PMP22.

(F) Representative scratch wound assay in healthy and DMD cells at day 10 (T0). Recolonization of the wound area is shown by the reduction of the blue/red area.

(G) Monitoring of the relative wound density (RWD) over time in the 3 DMD and 3 healthy control lines.

(H) The time to reach a relative wound density of 50% (RWD T50) was determined in 2 independent experiments (each with N = 8 replicate wells per line). Values were then averaged per line and each of the 3 DMD and 3 control lines was represented as an individual point. * p value <0.05. See also Figure S5 and Table S6.

were mostly downregulated in DMD cells, with the exception of the protocadherin (*PCDH*) family, in which 8/9 genes were upregulated (*PCDH17, PCDHA2, PCDHA7, PCDHB18P, PCDHGA3, PCDHGA4, PCDHGA5,* and *PCDHGB3,* mean log FC = 1.5) and only 1 was downregulated (*PCDHA13,* log FC = −1.7). To evaluate the functional impact of cell junction gene dysregulation at day 10, the migration velocity of DMD somite progenitors was compared to healthy control cells with a scratch-wound assay. Cell migration was precisely quantified by the relative wound density (RWD), which measures the cell density in the initial wound area normalized by the density outside the wound area of the same well. Healthy control cells were shown to reach an RWD of 50% in 7.8 ± 0.5 h, and the wound area was almost entirely closed in the first 12 h (Figure 5F). Given this time frame, the impact of cell division was assumed minimal compared to the intrinsic cell migration. Temporal follow-up of wound area recolonization showed that DMD cells migrated 17% faster than healthy controls with RWD50 = 6.5 ± 0.1 h (p = 0.02), in agreement with the defective epithelialization and the predominance of a mesenchymal population (Figures 5G and 5H). Similarly, the time taken by DMD cells to restore a confluency of 50% in the wound area was 34% lower in DMD cells (6.5 ± 0.1 h vs. 9.5 ± 0.4 h in healthy controls, p = 0.007) (Figures S5B and S5C). These results strongly suggest that dystrophin deficiency has functional consequences during myogenic development, particularly when somite progenitors undergo successive cell state transitions resulting in delamination and colonization of future muscle territories.

Altogether, our study combines data from four unrelated DMD patient hiPSC lines and four healthy controls plus one isogenic DMD mutant and indicates that dystrophin deficiency leads to major dysregulations of cell junction gene families participating in cell state transitions during somite development. As a working model, dysregulated somitogenesis and aberrant cell migration may result in the developmental phenotypes previously observed in fetuses at risk of developing DMD (Figure 6).

DISCUSSION

Thanks to carefully defined differentiation protocols, hiPSCs and their derivatives can help better understand human embryonic development and investigate the early impact of mutations leading to specific genetic disorders without the use of embryos.[14] Using a published protocol recapitulating key developmental steps of human myogenesis, we provide here a temporally resolved dataset spanning ten time points along the differentiation of healthy and DMD hiPSCs from pluripotency to the skeletal muscle lineage. Pluripotent cells first go through intensive transcriptional changes as they leave pluripotency and adopt an early mesodermal fate. After day 7, they stabilize as they become somite progenitors and their progenies (i.e., dermomyotome and skeletal muscle cells). The developmental trajectory computed from pseudotime data showed that fractions of cells reach the end of the myogenic process as early as day 10, reflecting the fact that differentiation is heterogeneous and asynchronous.[33,50,51] During the second half of the differentiation process, cells that are "behind schedule" probably "catch up" or remain stalled on an abortive developmental path. At the differentiation end stage, a majority of cells did not express canonical myogenic markers such as *MYOD1, MYOG,* or *PAX7.* However, most of them were positive for the myocyte-specific enhancer factor 2C (*MEF2C*), known to be involved not only in myogenesis but also in the development of a myriad of other tissues (i.e., heart, nervous system, vasculature, bone, and cartilage).[52] Neural cells have already been identified as cellular by-products generated alongside muscle cells with the myogenic differentiation protocol used in the first part of this study.[37] For this reason, a commercial myogenic media known to produce more homogeneous cell populations at the successive developmental steps was used in the subsequent steps of this study[17,20,53] (Table S4). This allowed us to confirm that similar to what is seen in DMD patients, the absence of dystrophin does not compromise the ability of hiPSCs to differentiate into myotubes. However, it may delay differentiation and/or deflect a fraction of cells from the skeletal muscle into alternative or abortive lineages during embryogenesis, which might go unnoticed *in vitro* due to the amplification and passage steps that are part of the differentiation protocols.

Here, we discovered that dystrophin mutation leads to the dysregulation of cell junctions during the successive cell state transitions which come with the *in vitro* differentiation of "somite-like" cell monolayers. Somites are transient metameric structures emerging from the paraxial mesoderm in the embryo. They give rise to multiple tissues such as the axial dermis, cartilages, bones, and skeletal muscles of the axis and limbs.[54,55] Individual somites are patterned along the dorsal-ventral axis into the sclerotome at the ventral pole and the dermomyotome at the dorsal pole. Myogenic progenitors delaminate from the dermomyotome to form primary multinucleated myofibers[12,56,57] (Figure 6). These
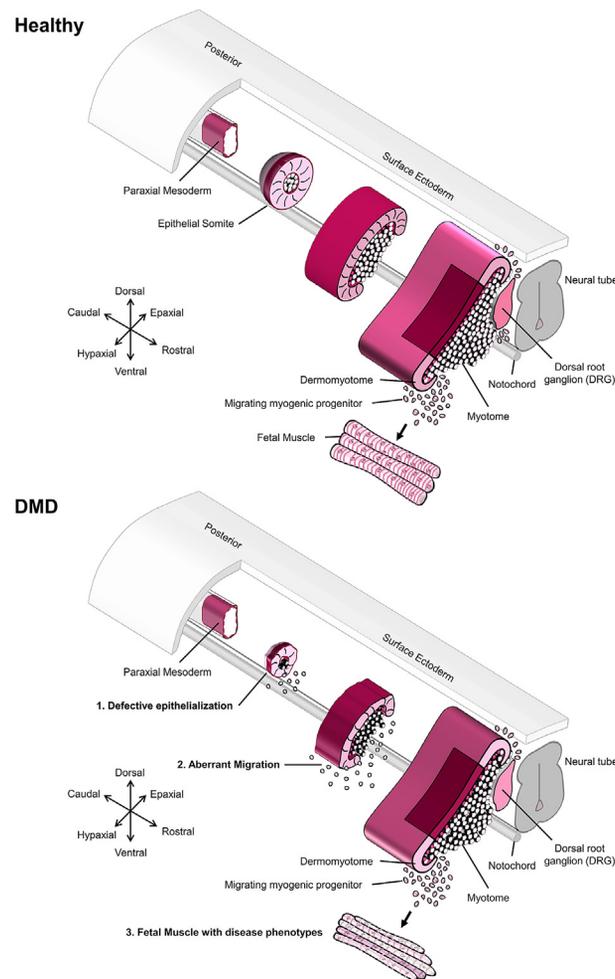
Figure 6. Working model of dysregulated somite development in DMD embryos

The top panel shows the successive steps of somitogenesis from the paraxial mesoderm in a healthy context, including the migration of myogenic progenitors colonizing the fetal muscle territories. In the bottom panel, the defective epithelialization and the aberrant migration phenotypes are highlighted in DMD somites, giving rise to fetal muscles with disease phenotypes, as previously published.[7,8]

developmental steps involve coordinated gene expression and successive transitions between a mesenchymal and an epithelial state.[10–12] We showed that the hiPSC model recapitulates key features of somitogenesis when subjected to myogenic differentiation, both at the level of their morphology and gene expression program. As a monolayer, somite progenitors derived from control hiPSCs spontaneously organize into discrete "epithelial islets", surrounded by mesenchymal cells. In the embryo, somite epithelialization requires the activity of *Paraxis* and the somites of *Paraxis*−/− murine embryos showed dysregulated somitogenesis and disorganized cell junctions.[11,58] The activity of the Rho family small GTPases Cdc42 and Rac1 also plays an essential role in the epithelialization during somitogenesis,[59] possibly by controlling the architecture of the cytoskeleton and the remodeling of cell junctions during the successive cell state transitions. Besides, cell junction proteins were massively associated with somite formation, segmentation, and specification in multiple species. For instance, cadherin 1, 2, 4, 5, 11, and 23 together with protocadherin 1, 8, and 18 were found expressed in developing somites of chicken embryos.[40] In the zebrafish, knockdown of cadherin 1 gene expression with morpholinos induced an aberrant somite morphology phenotype.[41] During somite segmentation in *Xenopus*, the activity of protocadherin 8/PAPC is required for segmentation,[42] and dominant negative forms of type I cadherins impaired the rotation of segmented somitomeres.[43] The role of PAPC in somite segmentation was later confirmed in chicken embryos, where it affects the epithelialization of mesoderm cells.[44] In the mouse embryo, N-cadherin and cadherin 11 were found expressed during the early steps of somite condensation from the paraxial mesoderm and then restricted to the dermomyotome and the sclerotome, respectively.[45] In addition, the removal of claudin 3, 4, and 8 led to irregularly shaped, fused somites, and defects in neural tube closure.[46] In this study, dystrophin deficiency in somite progenitors was linked with dysregulation of multiple cell junction genes including *CDH1*, *CDH2*, *CDH11*, *CLDN3*, and *CLDN4*, defective epithelialization, and increased migration (Figure 6). One appealing hypothesis would be that during somite development, the embryonic isoform of dystrophin serves as a stabilizing anchor for cell junction proteins in newly formed epithelial cells. Testing this hypothesis

will require further investigations in appropriate model systems, as Dp412e is specific to a subgroup of anthropoids, including humans, chimpanzees, gorillas, and orangutans.[21] Using our hiPSC model, we demonstrated that as a result of defective epithelialization, DMD progenitors have increased migration properties at the somite stage, which could in turn dysregulate the delamination process and the colonization of future skeletal muscle territories.

Multiple protein isoforms have been described from the *DMD* locus, each with a defined expression pattern,[60–62] but their function remains to be precisely characterized. In skeletal and cardiac muscles, the Dp427m dystrophin isoform is known to interact with the dystrophin-associated protein complex (DAPC), but in other tissues, the protein partners of other isoforms are less characterized. Recent studies have described association of dystrophin with alternative partners in specific cells and tissues, such as aquaporin 4, calcium, and potassium channels.[63–67] However, the exact molecular mechanisms driven by these interactions remain to be investigated. Dp412e was identified as an "embryonic" isoform induced during the formation of early mesoderm progenitors and embryoid bodies from hiPSCs.[21] The results of this study strongly suggest that Dp412e has specific roles during embryonic development and the cell transitions occurring when somites develop. In DMD patients, the absence of this isoform during the embryonic period might trigger a cascade of subtle molecular events leading to cellular phenotypes which only become apparent when the muscle tissue reaches a certain level of maturation. Reproducing *in vitro* the conditions in which skeletal muscle normally develops after birth will be critical to further characterize the dynamics of DMD using hiPSCs.

Altogether, our study leads us to consider DMD even more as a developmental disease, even though patients are born without apparent symptoms. A better understanding of the "invisible" DMD initiation events during development and early postnatal life will help identify biomarkers early in the course of disease progression, which in turn could accelerate diagnosis and pinpoint new therapeutic targets.

Limitations of the study

This study demonstrates the importance of the genetic background on the expressivity of the DMD mutation, as the transcriptome of the CRISPR line seemed less impacted by the mutation than in the DMD patient line. Thus, including more than one pair of isogenic hiPSC lines could increase the robustness of the data presented here. Integration of additional hiPSC lines from DMD patients and healthy controls and associated bulk RNA-seq datasets has helped strengthen the biological conclusions of this study, but these were not analyzed at the single-cell resolution. Additionally, our study includes a functional readout in the form of a cell migration assay to investigate the consequences of impaired cell junction formation during *in vitro* somitogenesis, but this is still far from reproducing the exact cell state transitions which occur in DMD embryos. Therefore, the mechanistic link connecting dystrophin deficiency to the altered dynamics of cell junctions during prenatal development of the skeletal muscle system and how it translates into disease phenotypes after birth remains hard to anticipate. In the absence of an appropriate animal model expressing the embryonic isoform of dystrophin, future studies should aim at exploiting even further the properties of 2D and 3D *in vitro* models based on patients-derived hiPSCs.

STAR★METHODS

Detailed methods are provided in the online version of this paper and include the following:

- KEY RESOURCES TABLE
- RESOURCE AVAILABILITY
  - Lead contact
  - Materials availability
  - Data and code availability
- EXPERIMENTAL MODEL AND STUDY PARTICIPANT DETAILS
  - Ethical statement
  - hiPSC lines
  - hiPSC maintenance
  - Rat muscle biopsies
- METHOD DETAILS
  - hiPSC myogenic differentiation
  - Single-cell RNA-Seq
  - Immunofluorescence
  - Western-blot
  - Cell migration assay
- QUANTIFICATION AND STATISTICAL ANALYSIS
  - Immunofluorescence
  - Cell migration assay

SUPPLEMENTAL INFORMATION

Supplemental information can be found online at https://doi.org/10.1016/j.isci.2024.110242.

AUTHOR CONTRIBUTIONS

Conceptualization: C.P., D.L.M., and J.B.D.; methodology: E.Mo, C.L., and J.B.D.; software: V.M., J.S.P., C.T., and J.B.D.; validation: E.Mo, C.L., and J.B.D.; formal analysis: E.Mo, C.L., and J.B.D.; investigation: E.Mo, E.Ma, V.M., C.L., A.B., D.L.J., and J.B.D.; resources: A.B., C.T., O.A., C.P., D.L.M., and J.B.D.; data curation: E.Mo, V.M., J.S.P., and J.B.D.; writing – original draft: E.Mo, C.L., and J.B.D.; writing – review and editing: E.Mo, E.Ma, V.M., C.L., C.T., C.L.G., O.A., C.P., D.L.M., and J.B.D.; visualization: E.Mo, C.L., J.S., and J.B.D.; supervision: C.T., C.L.G., O.A., C.P., D.L.M., and J.B.D.; project administration: J.B.D.; funding acquisition: E.Ma, V.M., O.A., C.P., D.L.M., and J.B.D.

DECLARATION OF INTERESTS

The authors declare no competing interests.

REFERENCES

1. Bushby, K., Finkel, R., Birnkrant, D.J., Case, L.E., Clemens, P.R., Cripe, L., Kaul, A., Kinnett, K., McDonald, C., Pandya, S., et al. (2010). Diagnosis and management of Duchenne muscular dystrophy, part 1: diagnosis, and pharmacological and psychosocial management. Lancet Neurol. 9, 77–93. https://doi.org/10.1016/S1474-4422(09)70271-6.

2. Wang, C.H., Bonnemann, C.G., Rutkowski, A., Sejersen, T., Bellini, J., Battista, V., Florence, J.M., Schara, U., Schuler, P.M., Wahbi, K., et al. (2010). Consensus statement on standard of care for congenital muscular dystrophies. J. Child Neurol. 25, 1559–1581. https://doi.org/10.1177/0883073810381924.

3. Wang, C.H., Dowling, J.J., North, K., Schroth, M.K., Sejersen, T., Shapiro, F., Bellini, J., Weiss, H., Guillet, M., Amburgey, K., et al. (2012). Consensus statement on standard of care for congenital myopathies. J. Child Neurol. 27, 363–382. https://doi.org/10.1177/0883073812436605.

4. Duan, D., Goemans, N., Takeda, S., Mercuri, E., and Aartsma-Rus, A. (2021). Duchenne muscular dystrophy. Nat. Rev. Dis. Primers 7, 13–19. https://doi.org/10.1038/s41572-021-00248-3.

5. Nguyen, F., Cherel, Y., Guigand, L., Goubault-Leroux, I., and Wyers, M. (2002). Muscle lesions associated with dystrophin deficiency in neonatal golden retriever puppies. J. Comp. Pathol. 126, 100–108. https://doi.org/10.1053/jcpa.2001.0526.

6. Merrick, D., Stadler, L.K.J., Larner, D., and Smith, J. (2009). Muscular dystrophy begins early in embryonic development deriving from stem cell loss and disrupted skeletal muscle formation. Dis. Model. Mech. 2, 374–388. https://doi.org/10.1242/dmm.001008.

7. Toop, J., and Emery, A.E. (1974). Muscle histology in fetuses at risk for Duchenne muscular dystrophy. Clin. Genet. 5, 230–233.

8. Emery, A.E. (1977). Muscle histology and creatine kinase levels in the foetus in Duchenne muscular dystrophy. Nature 266, 472–473. https://doi.org/10.1038/266472a0.

9. Pourquié, O., Al Tanoury, Z., and Chal, J. (2018). The Long Road to Making Muscle In Vitro. Curr. Top. Dev. Biol. 129, 123–142. https://doi.org/10.1016/bs.ctdb.2018.03.003.

10. Linker, C., Lesbros, C., Gros, J., Burrus, L.W., Rawls, A., and Marcelle, C. (2005). beta-Catenin-dependent Wnt signalling controls the epithelial organisation of somites through the activation of paraxis. Development 132, 3895–3905. https://doi.org/10.1242/dev.01961.

11. Rowton, M., Ramos, P., Anderson, D.M., Rhee, J.M., Cunliffe, H.E., and Rawls, A. (2013). Regulation of mesenchymal-to-epithelial transition by PARAXIS during somitogenesis. Dev. Dyn. 242, 1332–1344. https://doi.org/10.1002/dvdy.24033.

12. Zhou, Y., Zhang, Y., and Zhu, D. (2018). Myostatin promotes the epithelial-to-mesenchymal transition of the dermomyotome during somitogenesis. Dev. Dyn. 247, 1241–1252. https://doi.org/10.1002/dvdy.24681.

13. Mack, D.L., Guan, X., Wagoner, A., Walker, S.J., and Childers, M.K. (2014). Disease-in-a-dish: the contribution of patient-specific induced pluripotent stem cell technology to regenerative rehabilitation. Am. J. Phys. Med. Rehabil. 93, S155–S168. https://doi.org/10.1097/PHM.0000000000000141.

14. Avior, Y., Sagi, I., and Benvenisty, N. (2016). Pluripotent stem cells in disease modelling and drug discovery. Nat. Rev. Mol. Cell Biol. 17, 170–182. https://doi.org/10.1038/nrm.2015.27.

15. Karagiannis, P., Takahashi, K., Saito, M., Yoshida, Y., Okita, K., Watanabe, A., Inoue, H., Yamashita, J.K., Todani, M., Nakagawa, M., et al. (2019). Induced Pluripotent Stem Cells and Their Use in Human Models of Disease and Development. Physiol. Rev. 99, 79–114. https://doi.org/10.1152/physrev.00039.2017.

16. Chal, J., Al Tanoury, Z., Hestin, M., Gobert, B., Aivio, S., Hick, A., Cherrier, T., Nesmith, A.P., Parker, K.K., and Pourquié, O. (2016). Generation of human muscle fibers and satellite-like cells from human pluripotent stem cells in vitro. Nat. Protoc. 11, 1833–1850. https://doi.org/10.1038/nprot.2016.110.

17. Caron, L., Kher, D., Lee, K.L., McKernan, R., Dumevska, B., Hidalgo, A., Li, J., Yang, H., Main, H., Ferri, G., et al. (2016). A Human Pluripotent Stem Cell Model of Facioscapulohumeral Muscular Dystrophy-Affected Skeletal Muscles. Stem Cells Transl. Med. 5, 1145–1161. https://doi.org/10.5966/sctm.2015-0224.

18. Choi, I.Y., Lim, H., Estrellas, K., Mula, J., Cohen, T.V., Zhang, Y., Donnelly, C.J., Richard, J.-P., Kim, Y.J., Kim, H., et al. (2016). Concordant but Varied Phenotypes among Duchenne Muscular Dystrophy Patient-Specific Myoblasts Derived using a Human iPSC-Based Model. Cell Rep. 15, 2301–2312. https://doi.org/10.1016/j.celrep.2016.05.016.

19. Xi, H., Fujiwara, W., Gonzalez, K., Jan, M., Liebscher, S., Van Handel, B., Schenke-Layland, K., and Pyle, A.D. (2017). In Vivo Human Somitogenesis Guides Somite

Development from hPSCs. Cell Rep. *18*, 1573–1585. https://doi.org/10.1016/j.celrep.2017.01.040.

20. Mournetas, V., Massouridès, E., Dupont, J.-B., Kornobis, E., Polvèche, H., Jarrige, M., Dorval, A.R.L., Gosselin, M.R.F., Manousopoulou, A., Garbis, S.D., et al. (2021). Myogenesis modelled by human pluripotent stem cells: a multi-omic study of Duchenne myopathy early onset. J. Cachexia Sarcopenia Muscle *12*, 209–232. https://doi.org/10.1002/jcsm.12665.

21. Massouridès, E., Polentes, J., Mangeot, P.-E., Mournetas, V., Nectoux, J., Deburgrave, N., Nusbaum, P., Leturcq, F., Popplewell, L., Dickson, G., et al. (2015). Dp412e: a novel human embryonic dystrophin isoform induced by BMP4 in early differentiated cells. Skelet. Muscle *5*, 40. https://doi.org/10.1186/s13395-015-0062-6.

22. Cao, J., Spielmann, M., Qiu, X., Huang, X., Ibrahim, D.M., Hill, A.J., Zhang, F., Mundlos, S., Christiansen, L., Steemers, F.J., et al. (2019). The single-cell transcriptional landscape of mammalian organogenesis. Nature *566*, 496–502. https://doi.org/10.1038/s41586-019-0969-x.

23. Xi, H., Langerman, J., Sabri, S., Chien, P., Young, C.S., Younesi, S., Hicks, M., Gonzalez, K., Fujiwara, W., Marzi, J., et al. (2020). A Human Skeletal Muscle Atlas Identifies the Trajectories of Stem and Progenitor Cells across Development and from Human Pluripotent Stem Cells. Cell Stem Cell *27*, 158–176.e10. https://doi.org/10.1016/j.stem.2020.04.017.

24. Giordani, L., He, G.J., Negroni, E., Sakai, H., Law, J.Y.C., Siu, M.M., Wan, R., Corneau, A., Tajbakhsh, S., Cheung, T.H., and Le Grand, F. (2019). High-Dimensional Single-Cell Cartography Reveals Novel Skeletal Muscle-Resident Cell Populations. Mol. Cell *74*, 609–621.e6. https://doi.org/10.1016/j.molcel.2019.02.026.

25. Dos Santos, M., Backer, S., Saintpierre, B., Izac, B., Andrieu, M., Letourneur, F., Relaix, F., Sotiropoulos, A., and Maire, P. (2020). Single-nucleus RNA-seq and FISH identify coordinated transcriptional activity in mammalian myofibers. Nat. Commun. *11*, 5102. https://doi.org/10.1038/s41467-020-18789-8.

26. De Micheli, A.J., Spector, J.A., Elemento, O., and Cosgrove, B.D. (2020). A reference single-cell transcriptomic atlas of human skeletal muscle tissue reveals bifurcated muscle stem cell populations. Skelet. Muscle *10*, 19. https://doi.org/10.1186/s13395-020-00236-3.

27. Kimmel, J.C., Yi, N., Roy, M., Hendrickson, D.G., and Kelley, D.R. (2021). Differentiation reveals latent features of aging and an energy barrier in murine myogenesis. Cell Rep. *35*, 109046. https://doi.org/10.1016/j.celrep.2021.109046.

28. Petrany, M.J., Swoboda, C.O., Sun, C., Chetal, K., Chen, X., Weirauch, M.T., Salomonis, N., and Millay, D.P. (2020). Single-nucleus RNA-seq identifies transcriptional heterogeneity in multinucleated skeletal myofibers. Nat. Commun. *11*, 6374. https://doi.org/10.1038/s41467-020-20063-w.

29. Chemello, F., Wang, Z., Li, H., McAnally, J.R., Liu, N., Bassel-Duby, R., and Olson, E.N. (2020). Degenerative and regenerative pathways underlying Duchenne muscular dystrophy revealed by single-nucleus RNA sequencing. SA *117*, 29691–29701. https://doi.org/10.1073/pnas.2018391117.

30. Saleh, K.K., Xi, H., Switzler, C., Skuratovsky, E., Romero, M.A., Chien, P., Gibbs, D., Gane, L., Hicks, M.R., Spencer, M.J., and Pyle, A.D. (2022). Single cell sequencing maps skeletal muscle cellular diversity as disease severity increases in dystrophic mouse models. iScience *25*, 105415. https://doi.org/10.1016/j.isci.2022.105415.

31. Scripture-Adams, D.D., Chesmore, K.N., Barthélémy, F., Wang, R.T., Nieves-Rodriguez, S., Wang, D.W., Mokhonova, E.I., Douine, E.D., Wan, J., Little, I., et al. (2022). Single nuclei transcriptomics of muscle reveals intra-muscular cell dynamics linked to dystrophin loss and rescue. Commun. Biol. *5*, 989. https://doi.org/10.1038/s42003-022-03938-0.

32. Taglietti, V., Kefi, K., Bronisz-Budzyńska, I., Mirciloglu, B., Rodrigues, M., Cardone, N., Coulpier, F., Periou, B., Gentil, C., Goddard, M., et al. (2022). Duchenne muscular dystrophy trajectory in R-DMDdel52 preclinical rat model identifies COMP as biomarker of fibrosis. Acta Neuropathol. Commun. *10*, 60. https://doi.org/10.1186/s40478-022-01355-2.

33. Trapnell, C., Cacchiarelli, D., Grimsby, J., Pokharel, P., Li, S., Morse, M., Lennon, N.J., Livak, K.J., Mikkelsen, T.S., and Rinn, J.L. (2014). The dynamics and regulators of cell fate decisions are revealed by pseudotemporal ordering of single cells. Nat. Biotechnol. *32*, 381–386. https://doi.org/10.1038/nbt.2859.

34. Qiu, X., Mao, Q., Tang, Y., Wang, L., Chawla, R., Pliner, H.A., and Trapnell, C. (2017). Reversed graph embedding resolves complex single-cell trajectories. Nat. Methods *14*, 979–982. https://doi.org/10.1038/nmeth.4402.

35. Guan, X., Mack, D.L., Moreno, C.M., Strande, J.L., Mathieu, J., Shi, Y., Markert, C.D., Wang, Z., Liu, G., Lawlor, M.W., et al. (2014). Dystrophin-deficient cardiomyocytes derived from human urine: new biologic reagents for drug discovery. Stem Cell Res. *12*, 467–480. https://doi.org/10.1016/j.scr.2013.12.004.

36. Cao, J., Packer, J.S., Ramani, V., Cusanovich, D.A., Huynh, C., Daza, R., Qiu, X., Lee, C., Furlan, S.N., Steemers, F.J., et al. (2017). Comprehensive single-cell transcriptional profiling of a multicellular organism. Science *357*, 661–667. https://doi.org/10.1126/science.aam8940.

37. Kim, J., Magli, A., Chan, S.S.K., Oliveira, V.K.P., Wu, J., Darabi, R., Kyba, M., and Perlingeiro, R.C.R. (2017). Expansion and Purification Are Critical for the Therapeutic Application of Pluripotent Stem Cell-Derived Myogenic Progenitors. Stem Cell Rep. *9*, 12–22. https://doi.org/10.1016/j.stemcr.2017.04.022.

38. Smith, A.S., Luttrell, S.M., Dupont, J.-B., Gray, K., Lih, D., Fleming, J.W., Cunningham, N.J., Jepson, S., Hesson, J., Mathieu, J., et al. (2022). High-throughput, real-time monitoring of engineered skeletal muscle function using magnetic sensing. J. Tissue Eng. *13*, 20417314221122127. https://doi.org/10.1177/20417314221122127.

39. Thiery, J.P., Acloque, H., Huang, R.Y.J., and Nieto, M.A. (2009). Epithelial-Mesenchymal Transitions in Development and Disease. Cell *139*, 871–890. https://doi.org/10.1016/j.cell.2009.11.007.

40. Roy, P., and Bandyopadhyay, A. (2014). Spatio-Temporally Restricted Expression of Cell Adhesion Molecules during Chicken Embryonic Development. PLoS One *9*, e96837. https://doi.org/10.1371/journal.pone.0096837.

41. Babb, S.G., and Marrs, J.A. (2004). E-cadherin regulates cell movements and tissue formation in early zebrafish embryos. Dev. Dyn. *230*, 263–277. https://doi.org/10.1002/dvdy.20057.

42. Kim, S.H., Jen, W.C., De Robertis, E.M., and Kintner, C. (2000). The protocadherin PAPC establishes segmental boundaries during somitogenesis in xenopus embryos. Curr. Biol. *10*, 821–830. https://doi.org/10.1016/s0960-9822(00)00580-7.

43. Giacomello, E., Vallin, J., Morali, O., Coulter, I.S., Boulekbache, H., Thiery, J.P., and Broders, F. (2002). Type I cadherins are required for differentiation and coordinated rotation in Xenopus laevis somitogenesis. Int. J. Dev. Biol. *46*, 785–792.

44. Chal, J., Guillot, C., and Pourquié, O. (2017). PAPC couples the segmentation clock to somite morphogenesis by regulating N-cadherin-dependent adhesion. Development *144*, 664–676. https://doi.org/10.1242/dev.143974.

45. Kimura, Y., Matsunami, H., Inoue, T., Shimamura, K., Uchida, N., Ueno, T., Miyazaki, T., and Takeichi, M. (1995). Cadherin-11 expressed in association with mesenchymal morphogenesis in the head, somite, and limb bud of early mouse embryos. Dev. Biol. *169*, 347–358. https://doi.org/10.1006/dbio.1995.1149.

46. Baumholtz, A.I., Simard, A., Nikolopoulou, E., Oosenbrug, M., Collins, M.M., Piontek, A., Krause, G., Piontek, J., Greene, N.D.E., and Ryan, A.K. (2017). Claudins are essential for cell shape changes and convergent extension movements during neural tube closure. Dev. Biol. *428*, 25–38. https://doi.org/10.1016/j.ydbio.2017.05.013.

47. Bladt, F., Riethmacher, D., Isenmann, S., Aguzzi, A., and Birchmeier, C. (1995). Essential role for the c-met receptor in the migration of myogenic precursor cells into the limb bud. Nature *376*, 768–771. https://doi.org/10.1038/376768a0.

48. Andermarcher, E., Surani, M.A., and Gherardi, E. (1996). Co-expression of the HGF/SF and c-met genes during early mouse embryogenesis precedes reciprocal expression in adjacent tissues during organogenesis. Dev. Genet. *18*, 254–266. https://doi.org/10.1002/(SICI)1520-6408(1996)18:3<254::AID-DVG6>3.0.CO;2-8.

49. Dietrich, S., Abou-Rebyeh, F., Brohmann, H., Bladt, F., Sonnenberg-Riethmacher, E., Yamaai, T., Lumsden, A., Brand-Saberi, B., and Birchmeier, C. (1999). The role of SF/HGF and c-Met in the development of skeletal muscle. Development *126*, 1621–1629.

50. Zhang, H., and Miller, R.H. (1995). Asynchronous differentiation of clonally related spinal cord oligodendrocytes. Mol. Cell. Neurosci. *6*, 16–31. https://doi.org/10.1006/mcne.1995.1003.

51. Pauklin, S., and Vallier, L. (2013). The Cell-Cycle State of Stem Cells Determines Cell Fate Propensity. Cell *155*, 135–147. https://doi.org/10.1016/j.cell.2013.08.031.

52. Dong, C., Yang, X.-Z., Zhang, C.-Y., Liu, Y.-Y., Zhou, R.-B., Cheng, Q.-D., Yan, E.-K., and Yin, D.-C. (2017). Myocyte enhancer factor 2C and its directly-interacting proteins: A review. Prog. Biophys. Mol. Biol. *126*, 22–30. https://doi.org/10.1016/j.pbiomolbio.2017.02.002.

53. Mérien, A., Tahraoui-Bories, J., Cailleret, M., Dupont, J.-B., Leteur, C., Polentes, J., Carteron, A., Polvèche, H., Concordet, J.-P.,

Pinset, C., et al. (2021). CRISPR gene editing in pluripotent stem cells reveals the function of MBNL proteins during human in vitro myogenesis. Hum. Mol. Genet. *31*, 41–56. https://doi.org/10.1093/hmg/ddab218.

54. Brent, A.E., and Tabin, C.J. (2002). Developmental regulation of somite derivatives: muscle, cartilage and tendon. Curr. Opin. Genet. Dev. *12*, 548–557. https://doi.org/10.1016/S0959-437X(02)00339-8.

55. Weldon, S.A., and Münsterberg, A.E. (2022). Somite development and regionalisation of the vertebral axial skeleton. Semin. Cell Dev. Biol. *127*, 10–16. https://doi.org/10.1016/j.semcdb.2021.10.003.

56. Ordahl, C.P., Berdougo, E., Venters, S.J., and Denetclaw, W.F. (2001). The dermomyotome dorsomedial lip drives growth and morphogenesis of both the primary myotome and dermomyotome epithelium. Development *128*, 1731–1744. https://doi.org/10.1242/dev.128.10.1731.

57. Gros, J., Manceau, M., Thomé, V., and Marcelle, C. (2005). A common somitic origin for embryonic muscle progenitors and satellite cells. Nature *435*, 954–958. https://doi.org/10.1038/nature03572.

58. Burgess, R., Rawls, A., Brown, D., Bradley, A., and Olson, E.N. (1996). Requirement of the paraxis gene for somite formation and musculoskeletal patterning. Nature *384*, 570–573. https://doi.org/10.1038/384570a0.

59. Nakaya, Y., Kuroda, S., Katagiri, Y.T., Kaibuchi, K., and Takahashi, Y. (2004). Mesenchymal-epithelial transition during somitic segmentation is regulated by differential roles of Cdc42 and Rac1. Dev. Cell *7*, 425–438. https://doi.org/10.1016/j.devcel.2004.08.003.

60. Feener, C.A., Koenig, M., and Kunkel, L.M. (1989). Alternative splicing of human dystrophin mRNA generates isoforms at the carboxy terminus. Nature *338*, 509–511. https://doi.org/10.1038/338509a0.

61. Bies, R.D., Phelps, S.F., Cortez, M.D., Roberts, R., Caskey, C.T., and Chamberlain, J.S. (1992). Human and murine dystrophin mRNA transcripts are differentially expressed during skeletal muscle, heart, and brain development. Nucleic Acids Res. *20*, 1725–1731. https://doi.org/10.1093/nar/20.7.1725.

62. Muntoni, F., Torelli, S., and Ferlini, A. (2003). Dystrophin and mutations: one gene, several proteins, multiple phenotypes. Lancet Neurol. *2*, 731–740. https://doi.org/10.1016/S1474-4422(03)00585-4.

63. T, F., T, Y., H, T., and K, I. (2020). Dystroglycan regulates proper expression, submembranous localization and subsequent phosphorylation of Dp71 through physical interaction. Hum. Mol. Genet. *29*. https://doi.org/10.1093/hmg/ddaa217.

64. Romo-Yáñez, J., Rodríguez-Martínez, G., Aragón, J., Siqueiros-Márquez, L., Herrera-Salazar, A., Velasco, I., and Montanez, C. (2020). Characterization of the expression of dystrophins and dystrophin-associated proteins during embryonic neural stem/progenitor cell differentiation. Neurosci. Lett. *736*, 135247. https://doi.org/10.1016/j.neulet.2020.135247.

65. Belmaati Cherkaoui, M., Vacca, O., Izabelle, C., Boulay, A.-C., Boulogne, C., Gillet, C., Barnier, J.-V., Rendon, A., Cohen-Salmon, M., and Vaillend, C. (2021). Dp71 contribution to the molecular scaffold anchoring aquaporine-4 channels in brain macroglial cells. Glia *69*, 954–970. https://doi.org/10.1002/glia.23941.

66. Fujimoto, T., Stam, K., Yaoi, T., Nakano, K., Arai, T., Okamura, T., and Itoh, K. (2023). Dystrophin Short Product, Dp71 Interacts with AQP4 and Kir4.1 Channels in the Mouse Cerebellar Glial Cells in Contrast to Dp427 at Inhibitory Postsynapses in the Purkinje Neurons. Mol. Neurobiol. *60*, 3664–3677.

https://doi.org/10.1007/s12035-023-03296-w.

67. Leyva-Leyva, M., Sandoval, A., Morales-Lázaro, S.L., Corzo-López, A., Felix, R., and González-Ramírez, R. (2023). Identification of Dp140 and α1-syntrophin as novel molecular interactors of the neuronal CaV2.1 channel. Pflugers Arch. *475*, 595–606. https://doi.org/10.1007/s00424-023-02803-1.

68. Schindelin, J., Arganda-Carreras, I., Frise, E., Kaynig, V., Longair, M., Pietzsch, T., Preibisch, S., Rueden, C., Saalfeld, S., Schmid, B., et al. (2012). Fiji: an open-source platform for biological-image analysis. Nat. Methods *9*, 676–682. https://doi.org/10.1038/nmeth.2019.

69. Bankhead, P., Loughrey, M.B., Fernández, J.A., Dombrowski, Y., McArt, D.G., Dunne, P.D., McQuaid, S., Gray, R.T., Murray, L.J., Coleman, H.G., et al. (2017). QuPath: Open source software for digital pathology image analysis. Sci. Rep. *7*, 16878. https://doi.org/10.1038/s41598-017-17204-5.

70. Dobin, A., Davis, C.A., Schlesinger, F., Drenkow, J., Zaleski, C., Jha, S., Batut, P., Chaisson, M., and Gingeras, T.R. (2013). STAR: ultrafast universal RNA-seq aligner. Bioinformatics *29*, 15–21. https://doi.org/10.1093/bioinformatics/bts635.

71. Wickham, H., François, R., Henry, L., Müller, K., and Vaughan, D. (2023). dplyr: A Grammar of Data Manipulation. R package version 1.1.4, https://github.com/tidyverse/dplyr, https://dplyr.tidyverse.org.

72. (2016). ggplot2: Elegant Graphics for Data Analysis (New York: Springer-Verlag).

73. Bourdon, A., François, V., Zhang, L., Lafoux, A., Fraysse, B., Toumaniantz, G., Larcher, T., Girard, T., Ledevin, M., Lebreton, C., et al. (2022). Evaluation of the dystrophin carboxy-terminal domain for micro-dystrophin gene therapy in cardiac and skeletal muscles in the DMDmdx rat model. Gene Ther. *29*, 520–535. https://doi.org/10.1038/s41434-022-00317-6.

STAR★METHODS

KEY RESOURCES TABLE

REAGENT or RESOURCE	SOURCE	IDENTIFIER
Antibodies		
Myosin heavy chain	DSHB	Cat# MF20 RRID:AB_2147781
alpha-Actinin (Sarcomeric)	Sigma-Aldrich	Cat# A7811; RRID:AB_476766
CD324 (E-cadherin) Alexa Fluor™ 488	Thermo Fisher	Cat# 53-3249-80 RRID:AB_10671270
Vimentin eFluor™ 570	Thermo Fisher	Cat# 41-9897-80 RRID:AB_11220476
Human HGFR/c-MET	R&D Systems	Cat# AF276 RRID:AB_355289
Goat anti-Mouse IgG2b Alexa Fluor™ 555	Thermo Fisher	Cat# A-21147 RRID:AB_2535783
Donkey anti-Goat IgG Alexa Fluor™ 488	Thermo Fisher	Cat# A-11055 RRID:AB_2534102
Dystrophin	Leica	Cat# NCL-DYS2 RRID:AB_442081
GAPDH	Novus	Cat# NB300-320 RRID:AB_10001796
Alpha tubulin	Sigma-Aldrich	Cat# T5168 RRID:AB_477579
Goat Anti-Mouse Immunoglobulins/HRP	Agilent	Cat# P0447 RRID:AB_2617137
Polyclonal Rabbit Anti-Goat Immunoglobulins/HRP	Agilent	Cat# P0449 RRID:AB_2617143
Chemicals, peptides, and recombinant proteins		
mTeSR™ Plus	STEMCELL Technologies	Cat# 100-0276
Matrigel® Matrix	Corning	Cat# 354234
Versene solution	Thermo Fisher	Cat# 15040066
CryoStor CS10 cryopreservation medium	STEMCELL Technologies	Cat# 07959
DPBS	Thermo Fisher	Cat# 14190144
Y-27632 ROCK inhibitor	Selleckchem	Cat# S1049
DMEM/F12	Thermo Fisher	Cat# 11320033
CHIR99021	STEMCELL Technologies	Cat# 72054
StemMACS™ LDN-193189	Miltenyi Biotec	Cat# 130-103-925
Recombinant Human FGF2	R&D Systems	Cat# 233-FB-010
Recombinant Human IGF-1	R&D Systems	Cat# 291-G1-200
Recombinant Human HGF	R&D Systems	Cat# 294-HG-005
KnockOut™ serum replacement	Thermo Fisher	Cat# 10828010
Collagenase, type IV	Thermo Fisher	Cat# 1710419
Trypsin-EDTA	Sigma-Aldrich	Cat# T4174
Skeletal Muscle. Induction Medium	amsbio	Cat# SKM01
Skeletal Muscle. Myoblast Medium	amsbio	Cat# SKM02
Skeletal Muscle. Myotube Medium	Amsbio	Cat# SKM03
Cultrex Rat Collagen I	R&D Systems	Cat# 3440-100-01
Paraformaldehyde	Thermo Fisher	Cat# #28906
Triton 100X	Eurobio	Cat# GAUTTR001
BSA (immunofluorescence)	Sigma-Aldrich	Cat# A3059
ProLong™ Gold Antifade reagent	Thermo Fisher	Cat# P36934
Tris base	Sigma-Aldrich	Cat# 10708976001
cOmplete™ Protease Inihibitor Cocktail	Merck	Cat# 11873580001
Protease inhibitor cocktail	Sigma-Aldrich	Cat# P8340
Igepal CA-630	Sigma-Aldrich	Cat# I3021

(Continued on next page)

Continued

REAGENT or RESOURCE	SOURCE	IDENTIFIER
SDS solution	Sigma-Aldrich	Cat# 05030
NuPAGE™ LDS sample buffer	Thermo Fisher	Cat# NP0007
Dithiothreitol	Thermo Fisher	Cat# D1532
NuPAGE™ Tris-acetate Gel	Thermo Fisher	Cat# EA03785BOX
NuPAGE™ Tris acetate SDS buffer	Thermo Fisher	Cat# LA0041
Tween 20	Merck	Cat# 8170721000
Pierce™ ECL Western Blotting Substrate	Thermo Fisher	Cat# 32106
Nuclease free water	Ambion	Cat# AM9932
Methanol	Fisher Scientific	Cat# 10285131
SUPERase In RNase inhibitor	Invitrogen	Cat# AM2694
BSA (single-cell RNA-Seq)	New England Biolabs	Cat# B9000
1M Tris-HCl pH 7.5	Thermo Fisher	Cat# 15567027
5M NaCl (single-cell RNA-Seq)	Thermo Fisher	Cat# AM9759
1M MgCl2	Thermo Fisher	Cat# AM9530G
IGEPAL CA-360	Sigma-Aldrich	Cat# 18896
Diethyl pyrocarbonate	Sigma-Aldrich	Cat# D5758
10 mM dNTP	Thermo Fisher	Cat# 18427013
Superscript IV reverse transcriptase	Thermo Fisher	Cat# 18090200
RNaseOUT Recombinant Ribonuclease Inhibitor	Thermo Fisher	Cat#10777019
0.5M EDTA pH 8.0	Thermo Fisher	Cat# 15575020
Spermidine	MP Biomedicals	Cat# 0219485201
Elution Buffer	Qiagen	Cat# 19086
DAPI	Thermo Fisher	Cat# D1306
DNA binding buffer	Zymo Research	Cat# D4003-1
AMPure XP beads	Beckman Coulter	Cat# A63880
Ethanol	Decon Labs	Cat# 2716
NEBNext® High Fidelity 2X PCR Master Mix	New England Biolabs	Cat# M0541
Novex® TBE-PAGE gels, 6%	Thermo Fisher	Cat# EC6265BOX
Quick-Load 2-log DNA Ladder	New England Biolabs	Cat# N0550
Critical commercial assays		
Nextseq 500/550 V2 75 cycle kit	illumina	Cat# 20024906
DC Protein Assay	Bio-Rad	Cat# 5000111
Tagment DNA TDE1 Enzyme and Buffer Kit	illumina	Cat# 20034197
Evercode™ Whole Transcriptome Mini Kit	Parse Biosciences	Cat# EC-W01010
Cell Fixation Kit	Parse Biosciences	Cat# SB1001
Qubit dsDNA HS Kit	Thermo Fisher	Cat# Q32851
NEBNext® Ultra™ II Non-Directional RNA Second Strand Synthesis Module	New England Biolabs	Cat# E6111
Deposited data		
sciRNA-Seq myogenesis time course data	This paper	GEO: GSE233605
Bulk RNA Seq Day 10 data	Mournetas et al.[20]	ArrayExpress: E-MTAB-8321
Split-pool barcoding scRNASeq Day 10 data	This paper	GEO: GSE233606
Tables S1, S2, S3, S4, S5, S6, and S7	This paper	Zenodo: https://doi.org/10.5281/zenodo.10849178

Continued

REAGENT or RESOURCE	SOURCE	IDENTIFIER
Full Western blots films related to Figure S2A	This paper	Zenodo: https://doi.org/10.5281/zenodo.7937310
Immunofluorescence pictures related to Figures 3A and 3B	This paper	Zenodo: https://doi.org/10.5281/zenodo.8325281
Immunofluorescence pictures related to Figures 4B and 4C	This paper	Zenodo: https://doi.org/10.5281/zenodo.7950222
Immunofluorescence pictures related to Figures 4D and 4E	This paper	Zenodo: https://doi.org/10.5281/zenodo.8325290
Immunofluorescence pictures related to Figures 5A and 5B	This paper	Zenodo: https://doi.org/10.5281/zenodo.8325317
Experimental models: Cell lines		
UC3-4 Healthy hiPSC line, passage 32	Laboratory of David L Mack	N/A
DMD 72039 D3 hiPSC line, passage 22	Laboratory of David L Mack	N/A
UC3-4 DMD CRISPR hiPSC line, passage 41	Laboratory of David L Mack	N/A
NIH/3T3 cell spike (single-cell RNA-Seq)	ATCC	N/A
Oligonucleotides		
sciRNA-Seq barcoded oligonucleotides (see Table S1)	IDT	N/A
Custom P5 and P7 primers (see Table S1)	IDT	N/A
Software and algorithms		
Fiji (ImageJ)	Schindelin et al.[68]	https://fiji.sc/
QuPath version 0.4.3	Bankhead et al.[69]	https://qupath.github.io/
PRISM version 8	Graphpad	https://www.graphpad.com/features
bcl2fastq version 2.16.0.10	illumina	https://emea.support.illumina.com/sequencing/sequencing_software/bcl2fastq-conversion-software.html
trim_galore version 0.4.5	Felix Krueger	https://www.bioinformatics.babraham.ac.uk/projects/trim_galore/
STAR version 2.5.2b	Dobin et al.[70]	https://github.com/alexdobin/STAR
R version 4.2.2	https://cran.r-project.org/	
dplyr version 1.1.0	Wickham et al.[71]	https://dplyr.tidyverse.org/
monocle version 1.3.1	Cao et al.[22,36]	https://cole-trapnell-lab.github.io/monocle3/
ggplot2 version 3.1.4	Wickham et al.[72]	https://ggplot2.tidyverse.org/
sci-RNA-Seq and split-pool barcoding analysis pipelines	This paper	Zenodo https://doi.org/10.5281/zenodo.8348000

RESOURCE AVAILABILITY

Lead contact

Further information and requests for resources and reagents should be directly addressed to and will be fulfilled by the lead contact, Jean-Baptiste Dupont (jean-baptiste.dupont@univ-nantes.fr).

Materials availability

This study did not generate new unique reagents.

Data and code availability

- The two single-cell RNA-seq datasets have been deposited at GEO and are publicly available as of the date of publication. Accession numbers are listed in the key resources table. This paper also analyzes publicly available data. These accession numbers are listed in the

EXPERIMENTAL MODEL AND STUDY PARTICIPANT DETAILS

Ethical statement

The Healthy, DMD and CRISPR lines have been described, characterized and published previously.[20,35,38] Participants gave informed consent for the generation of urine-derived hiPSC lines, as required by the Institutional Review Board (IRB). The experiments performed in this manuscript fall into the Category 1A described in the Guidelines for Stem Cell Research and Clinical Translation of the International Society for Stem Cell Research (ISSCR, https://www.isscr.org/guidelines).

hiPSC lines

The Healthy UC3-4 line was generated from an adult male participant with no known skeletal muscle disease. The DMD 72039 line was generated from an adult male with a declared DMD pathology and carrying an exon50 deletion in the *DMD* gene. These individuals provided urine samples, from which urine cells were expanded and reprogrammed to generate hiPSCs by Guan X. et al. at the University of Washington, Seattle (USA).[35] The DMD CRISPR line was generated from the UC3-4 line by CRISPR Cas 9 gene editing by Smith A. et al. in collaboration with the Institute for Stem Cell and Regenerative Medicine Ellison Stem Cell Core.[38] It carries an exon 45 deletion and a 17 bp deletion in exon 54 of the *DMD* gene. The absence of dystrophin was confirmed by Western blot after myogenic differentiation, in comparison with the Healthy UC3-4 control line (Figure S2A). Cell lines were not otherwise authenticated. The three hiPSC lines were extensively characterized, expanded and shared with the TaRGeT INSERM laboratory at Nantes Université through a dedicated Material Transfer Agreement. The three additional DMD patient-derived hiPSC lines and the three additional healthy control lines were previously generated by Mournetas V. and Massouridès E. at the I-Stem institute, Corbeil-Essonnes (France).[20] The mutations are specified in Figure S4.

hiPSC maintenance

All cell culture experiments were performed at 37°C and 5% CO2 in a standard tissue culture incubator. The three hiPSC lines were expanded in the TaRGeT laboratory as Master Cell Banks (MCB) at various passages (Healthy: passage 34; DMD: passage 25; CRISPR: passage 46). Cells were thawed at 37°C and seeded as clusters on Matrigel-coated plates (1:60 dilution) after spinning 3 min at 300 g and resuspension in mTeSR Plus culture medium supplemented in 10 μM ROCK inhibitor. Fresh media without ROCK inhibitor was renewed the day after seeding and then every other day. Cultures were manually cleaned from abnormally looking clusters and were passaged with Versene when the overall confluence reached 70–80%. Working Cell Banks (WCB) were stored after two passages from the MCBs. Cells were detached with Versene, spun down 3 min at 300 g, and clusters were gently resuspended in Cryostor freezing media for long term cryopreservation in liquid nitrogen.

Rat muscle biopsies

The protein samples used as positive controls in the dystrophin western-blot were obtained from rat pectoral muscle biopsies from a previous study.[73] Dmd^mdx rats and healthy controls were handled and housed in the UTE IRS2 from Nantes Université, according to a protocol approved by the Institutional Animal Care and Use Committee of the Région des Pays de la Loire (University of Angers, France) as well as the French Ministry for National Education, Higher Education and Research (authorization #2018102616384887).

METHOD DETAILS

hiPSC myogenic differentiation

This study combines the use of two myogenic differentiation protocols.

(1) Establishment of the myogenic trajectory: hiPSCs were differentiated with a succession of five defined media, as published previously.[16] After seeding on Matrigel (1:60 dilution) as single cells at a density of 30,000 cells/cm^2, hiPSCs were grown for 2–3 days in mTeSR Plus media. ROCK inhibitor was added upon seeding but removed by a fresh media change after one day. The cells were then incubated in five successive differentiation media based on Dulbecco's Modified Eagle's Medium (DMEM)/F12 supplemented with Non-Essential Amino Acids (NEAA) and additional molecules detailed below:

Media 1 (3 days): Insulin transferrin selenium (ITS) 1X + 3 μM CHIR99021 + 0.5 μM LDN

Media 2 (3 days): Insulin transferrin selenium (ITS) 1X + 3 μM CHIR99021 + 0.5 μM LDN + basic Fibroblast Growth Factor (bFGF) at 20 μg/ml

Media 3 (2 days): 15% Knockout serum replacement (KSR) + 0.5 μM LDN + bFGF at 20 μg/mL + Hepatocyte Growth Factor (HGF) at 10 μg/mL + Insulin-like Growth Factor (IGF) 1 at 2 ng/mL.

Media 4 (4 days): 15% KSR + IGF-1 at 2 ng/ml

Media 5 (16 days): 15% KSR + IGF-1 at 2 ng/mL + HGF at 10 μg/mL

Cells were collected at Day 0, 1, 2, 4, 7, 10, 14, 18, 22 and 28 after incubation with Trypsin-EDTA alone, or with a combination of Trypsin-EDTA + collagenase IV at 50 U/μL for 10 min at 37°C, mechanical dissociation and passage through a 70 μm cell strainer to remove debris and extracellular matrix.

(1) Post hoc analysis of the somite differentiation stage at Day 10: in parallel, hiPSCs were differentiated with a commercially available media previously shown as capable of reproducing the somite stage with high accuracy.[17,20] This protocol uses lower initial seeding densities and allows for an easier visualization and imaging of the cultures as differentiation progresses. Briefly, hiPSCs were first amplified and dissociated as single cells as described above, and then seeded on collagen I-coated plates at 3,500 cells/cm^2 in Skeletal Muscle Induction Medium (amsbio SKM01). The media was changed every 2 to 3 days. At Day 7, cells were dissociated with Trypsin-EDTA and cryopreserved in CryoStor CS10 medium. They were seeded on new collagen-coated plates at 20,000 cells/cm^2 in SKM01 until Day 10.

Single-cell RNA-Seq

(1) sci-RNA-Seq: the myogenic trajectory followed by hiPSCs was determined by single-cell combinatorial indexing RNA-Seq (sci-RNA-Seq) as previously published.[36] Cells were collected as differentiation progressed (5–10 million per sample, from Day 0 to Day 28) and spiked with 10% murine cells of the NIH/3t3 cell line for estimation of doublet proportions. after centrifugation for 5 min at 300 g and 4°C, pellets were washed in DPBS and resuspended in pre-chilled methanol for fixation and permeabilization. They were then stored at – 20°C until all samples were processed at the end of the differentiation. Fixed cells were pelleted by centrifugation (same settings), washed twice in 1 mL DPBS +1% Diethylpyrocarbonate (DEPC), and another three times in 1 mL of cell wash buffer containing 1% SUPERase In RNase Inhibitor and 1% BSA in ice-cold DPBS. The final resuspension was made in 100 μL of cell wash buffer before counting with a hemocytometer. The Reverse Transcription step was performed 10 min at 55°C in situ on 2,000 cells per sample, with the Superscript IV RT kit and barcoded oligo dT primers dispatched in a Lo-bind 96-well plate. To increase the diversity of barcode combinations obtained after indexing, six distinct barcodes were used for the Day 0, Day 1 and Day 2 samples and four barcodes for the remaining samples (Day 4, Day 7, Day 10, Day 14, Day 18, Day 22, Day 28). The RT reaction was stopped with 40 mM EDTA and 1 mM spermidine (5 μL per well). Cells with barcoded cDNA were then pooled in a flow cytometry tube, stained with 300 μM DAPI and sorted in a new 96-well Lo-bind plate (25 cells per well) containing Elution buffer (5 μL per well). Sorting plates can be stored at – 80°C after brief centrifugation. Second strand synthesis was performed in each well with the NEBNext Ultra II Non-Directional RNA Second Strand Synthesis Module (0.5 μL of Buffer +0.25 μL of enzyme per well). After incubation at 16°C for 150 min, the reaction was terminated at 75°C for 20 min. Tagmentation was performed in each well with the illumina Tagment DNA TDE1 Enzyme (0.5 μL per well) and buffer (5 μL per well) kit, after addition of human genomic DNA (0.25 μL per well). The plate was incubated at 55°C for 5 min and the reaction was stopped with 12 μL DNA binding buffer per well and incubation at RT for 5 min. AMPure XP beads (36 μL per well) were added for purification with standard protocol. The elution step was performed in a final volume of 17 μL. Libraries were amplified by PCR using the NEBNext High-Fidelity 2X PCR Master Mix and barcoded P5 primers (2 μL of 10 μM primer per well), in addition to a 10 μM P7 primer (2 μL per well). Amplification was carried out in a standard thermal cycler with the following program: 5 min at 72°C + 30 s at 98°C + 18 cycles of (10 s at 98°C + 30 s at 66°C + 30 s at 72°C) + 5 min at 72°C. Samples were collected from each well and pooled in a single tube. The library was then purified using 0.8 volume of AMPure XP beads according to manufacturer's instructions. Libraries were quantified by Qubit and visualized by electrophoresis on a 6% TBE-PAGE gel. Sequencing was performed on the NextSeq 500 platform using a V2 75 cycles kit and the following settings: Read 1: 18 cycles, Read 2: 52 cycles, Index 1: 10 cycles, Index 2: 10 cycles. Here, two sorting plates were generated and used to generated independent libraries sequenced successively with distinct P7 primers. The first sorting plate was full and thus 96 barcoded P5 primers were used in the PCR amplification step; the second sorting plate only used 86 wells (and thus 86 barcoded P5 primers). The sequences of the barcoded primers used in this protocol can be found in Table S7. Raw data analysis involved base calling (bcl2fastq), demultiplexing based on P5 barcodes (1 mismatched base allowed), adapter trimming (trim_galore), alignment to the human (hg19) or the mouse (mm10) genome (STAR[70]), removing of UMI duplicates and demultiplexing based on RT barcodes. Percentages of reads mapping uniquely to the human and the mouse genome were quantified and cells with over 90% of reads assigned to the human genome were kept for subsequent analysis. Secondary analysis of the cell dataset object was performed with the Monocle 3 analysis pipeline (Trapnell 2014, Qiu 2017), whose code is freely available on the Cole Trapnell lab Github and in the Zenodo Repository with the DOI listed in the key resources table.

(2) split-pool barcoding: the post hoc analysis of the somite differentiation step at Day 10 was performed with the split-pool barcoding kit commercialized by parse Biosciences, according to manufacturer's instructions. Cells were collected at Day 10 and counted with a hemocytometer to isolate 500,000 cells for subsequent fixation and permeabilization with the Cell Fixation Kit. Samples were stored at – 80°C and thawed immediately prior to library preparation with the Evercode Whole Transcriptome Mini Kit. Primary analysis of the raw data including quality control, alignment to the human genome (hg19), demultiplexing and generation of the matrix, feature annotation and cell annotation files were carried out by the proprietary Parse Biosciences analysis suite. Secondary analysis used the Monocle 3 pipeline as previously indicated. The code has been deposited at Zenodo Repository with the DOI listed in the key resources table.

Immunofluorescence

(1) Somite progenitors: hiPSCs were first differentiated into somite progenitor cells with the amsbio commercial protocol to constitute a working cell bank at Day 7. Subsequently, cryotubes containing one million progenitors were thawed and seeded at 23,500 cells/cm^2 on Lab-Tek 4-well chamber slides (Thermofisher Cat# 154526PK) coated with collagen I (1:60 dilution). Cells were maintained in Skeletal Muscle Induction medium supplemented with 2% Pen/Strep and incubated at 37°C, 5% CO2 until confluency.

(2) Myotubes: myogenic progenitors were differentiated from hiSPCs with the amsbio commercial protocol and banks were made at Day 17. Subsequently, cryotubes containing one million progenitors were thawed and seeded at 23,500 cells/cm^2 on Lab-Tek 4-well chamber slides (Thermofisher Cat# 154526PK) coated with collagen I (1:60 dilution). They were maintained in Skeletal Muscle Myoblast medium supplemented with 2% Pen/Strep and incubated at 37°C, 5% CO2 until confluency. Differentiation was induced with the Skeletal Muscle Myotube medium supplemented with 2% Pen/Strep for 8 days, with a fresh media change every 2 to 3 days.

Cells were fixed in 4% paraformaldehyde (PFA) for 1 h and then permeabilized in PBS + Triton 1X + 2.5% bovine serum albumin (BSA). Primay antibodies were diluted in permeabilization buffer and incubated on the cells overnight at 4°C (E-Cadherin Alexa Fluor 488, Vimentin eFluor 570 and C-Met: 1:50 dilution; Myosin Heavy Chain: 1:300 dilution; α-actinin: 1:500 dilution). The next day, nuclei were stained with 1:10.000 DAPI and for myotubes, the anti-mouse or anti-goat (C-Met) secondary antibodies were diluted at 1:1000 in PBS and added for 1 h at RT. Coverslips were mounted on the slides using ProLong Gold Antifade Reagent after removing the Lab-Tek walls. Images were taken with a 20✕ oil immersion objective on a NIKON A1 RSi confocal microscope.

Western-blot

Proteins were extracted from frozen cell pellets in RIPA buffer during 1 h (10 mM Tris +150 Mm NaCl + 1 mM protease inhibitor cocktails +1% Igepal +0.1% SDS). Protein extracts diluted at 1:10 were quantified with the DC Protein Assay kit at 750 nm on the Thermo Scientific Multiskan GO. Protein samples (50 μg per sample) were denatured by addition of NuPAGE LDS sample buffer 4X and Dithiothreitol (DTT), and loaded onto a Nupage 3–8% TA Gel before migrating for 2 h at 100 V in 1X NuPAGE tris acetate SDS buffer. Protein extracts from Healthy and DMD^{mdx} rat pectoral muscles were loaded as controls. The Bio-Rad Trans-Blot Turbo Transfer System was used for protein transfer. After overnight saturation at 4°C in saturation buffer (5% milk +0.1% Tween 20 + 1% NP40), membranes were incubated with primary Mouse anti-dystrophin NCL-DYS2 antibody diluted at 1:250 for 1 h. The α-tubulin protein was labeled with a Mouse Monoclonal Anti-α-Tubulin antibody diluted at 1:10000. All membranes were then washed three times for 5 min in PBS +0.1% Tween 20 before incubation with the corresponding secondary antibodies (Goat Anti-Mouse antibody/HRP diluted at 1:5000 during 1 h). The ECL kit was used for detection of the HRP enzyme activity, with exposure times of 2 min (α-tubulin) and 2 h (Dystrophin).

Cell migration assay

Somite progenitors derived from hiPSCs were frozen and amplified at Day 7 of the amsbio SkM differentiation protocol. They were seeded in an Imagelock 96-well plate at 20,000 cells/cm^2 and grown in SkM01 medium for 3 days (8 wells per line). At Day 10, the Incucyte Woundmaker was used to create homogeneous wound in the cell monolayer, according to the manufacturer's instructions. Fresh SkM01 medium was added and the plate was plate in the Incucyte Live-Cell Analysis system for image acquisition in each well every hour for 24 h.

QUANTIFICATION AND STATISTICAL ANALYSIS

Immunofluorescence

Each hiPSC line was differentiated and imaged as 4 by 4 panels or individual pictures, and analyzed with the Fiji[68] or QuPath[69] softwares. C-Met and Ecad-positive areas were determined by thresholding on the Alexa 488 fluorescent channel (ECad: Threshold = 40 or regions manually drawn if low signal, C-Met: Threshold = 600, minimal object size = 2,500 μm^2), and the number of nuclei was determined in the positive and negative areas using the Cell Detection tool with the following parameters: C-Met: DAPI threshold = 100, object size between 10 and 400 μm^2, background radius = 8 μm, sigma = 1.5 μm; E-Cad: DAPI threshold = 100, object size between 75 and 2000 μm^2, background radius = 8 μm, sigma = 2 μm. E-Cad pictures were acquired at higher magnification, explaining why different parameters had to be used. MF20- and α-actinin-positive areas were determined by thresholding on the TRITC channel (MF20: threshold = 100, α-actinin: threshold = 1000). Data were represented and analyzed with GraphPad PRISM 8.0.1. Non-parametric statistical tests were used to compare groups as sample size were low and we could not assume Gaussian distributions nor homoscedasticity. The Mann-Whitney statistics was used when only two groups were compared, and the Kruskal-Wallis statistics with Dunn's multiple comparison test for comparison of the 3 groups.

Cell migration assay

Data processing and determination of the relative wound density over time was performed with the dedicated Incucyte analysis module. As previously mentioned, two independent experiments were performed and the data were pooled for statistical analysis (Mann-Withney U-test). Each experiment included Day 7 progenitors derived from 6 hiPSC lines (3 Healthy and 3 DMD), each seeded in 8 wells of the Imagelock 96-well plate. Each hour, data points were collected in each well, and the RWD and WC of each line was determined by averaging the data of the 8 wells.